Effective-Hamiltonian Theory of Open Quantum Systems at Strong Coupling

Nicholas Anto-Sztrikacs,[1] Ahsan Nazir,[2] and Dvira Segal[1,3,*]

[1] *Department of Physics, University of Toronto, 60 Saint George Street, Toronto, Ontario M5S 1A7, Canada*

[2] *Department of Physics and Astronomy, University of Manchester, Oxford Road, Manchester M13 9PL, United Kingdom*

[3] *Chemical Physics Theory Group, Department of Chemistry and Centre for Quantum Information and Quantum Control, University of Toronto, 80 Saint George St., Toronto, Ontario, M5S 3H6, Canada*

(Received 12 November 2022; accepted 6 March 2023; published 13 April 2023)

We present the reaction-coordinate polaron-transform (RCPT) framework for generating effective-Hamiltonian models to treat nonequilibrium open quantum systems at strong coupling with harmonic environments. Our approach, which is based on two exact transformations of the Hamiltonian followed by its controlled truncation, ends with a new Hamiltonian with a weakened coupling to the environment. This new effective Hamiltonian mirrors the initial one, except that its parameters are dressed by the system-bath couplings. The power and elegance of the RCPT approach lie in its generality and in its mathematical simplicity, allowing for analytical work and thus profound understanding of the impact of strong system-bath coupling effects on open-quantum-system phenomena. Examples interrogated in this work include canonical models for quantum thermalization, charge and energy transport at the nanoscale, and performance bounds of quantum thermodynamical machines such as absorption refrigerators and thermoelectric generators, as well as the equilibrium and nonequilibrium behavior of many-body dissipative spin chains.

DOI: 10.1103/PRXQuantum.4.020307

I. INTRODUCTION

Quantum systems are inevitably coupled to their surrounding environment. At the nanoscale, these interactions are influential and cannot be neglected, which in turn leads to theoretical and technical challenges in modeling open quantum systems. Quantum master-equation (QME) approaches offer a powerful framework for simulating open quantum systems. While the Nakajima-Zwanzig formalism is exact [1], approximations must be made for practical computations. Most commonly, QMEs are made perturbative in the system-bath coupling parameter; the prominent Redfield equation takes into account only the lowest (second) nontrivial order in this expansion, referred to as the Born approximation. Weak-coupling QMEs offer straightforward computations and analytical results in some cases and as such they have gained enormous popularity in diverse fields: e.g., chemical dynamics [1], quantum optics [2], quantum information science [3,4], and quantum thermodynamics [5,6]. However, these methods are strictly limited to the weak-coupling regime, missing rich physics. This work presents a Hamiltonian reformation (transformation and truncation) technique that allows the treatment of strong-coupling regimes while providing both a detailed understanding of such effects in quantum systems and a cheap route for computations.

The applications detailed in this work concern quantum transport and quantum thermodynamics problems [5–12], where a consistent theory of thermodynamics in the quantum regime relies on the correct treatment of strong-coupling features. However, our approach can be exercised on other open problems in a variety of contexts.

Focusing on quantum thermodynamics in the context of thermal machines, strong-coupling effects can allow nonclassical correlations to build up between the system and its reservoirs, which could be utilized as a resource to design novel quantum technologies [13,14]. While it is debated whether strong-coupling effects are beneficial or detrimental to their performance [15–18], it is clear that strong-coupling effects can significantly impact the performance and efficiency of thermal devices by, e.g., renormalizing parameters and opening up new transport pathways [19–21]. Additionally, in the context of thermalization, strong system-bath interactions lead to deviations from the canonical distribution, which is predicted to hold under the assumption of vanishingly weak system-reservoir coupling [13,22–35]. Strong coupling is also responsible for deviations from simple additivity approximations [36–38].

*dvira.segal@utoronto.ca

To capture such nontrivial effects, one must go beyond second-order perturbative QMEs. One such choice is to use numerically exact methods, including the multiconfiguration time-dependent Hartree (MCTDH) approach [39–41], numerical renormalization-group methods [42–44], the hierarchical equations of motion [45,46], path-integral approaches [47–55], quantum Monte Carlo algorithms [56–58], chain-mapping techniques [59–62], tensor-network-based methods [63], and more. Strong-coupling effects have also been investigated by studying the full density matrix dynamics, an approach that is particularly useful for driven systems [14–16,64–66]. Although numerically exact methods provide accurate benchmarks for describing open quantum systems at strong coupling, (i) they are often limited to minimal models and (ii) they fail to provide analytical intuition and, hence, do not allow us to pursue the objective of this work: to understand the fundamental essence of strong coupling.

Conversely, there exist other inexact tools that allow the development of analytical understanding. These include the noninteracting-blip approximation (NIBA), which is applicable for Ohmic spectral functions [67–69], the polaron-transformed Redfield equation, which allows for more general spectral functions [70–74], and Green's function techniques [75–81]. However, typically, these tools immediately become cumbersome beyond minimal models and are restricted in their applicability since they are perturbative in some parameters.

The reaction-coordinate (RC) mapping [13,82–85] bridges the gap between powerful numerical tools and low-order perturbative analytical methods. While originally developed in the context of chemical reactivity [84,85], in recent years the method has found numerous applications in the context of quantum thermodynamics as a general tool to capture the effects of strong system-reservoir coupling. In this technique, a central collective degree of freedom from the reservoir is extracted and included as part of the system. The original quantum system is then extended and termed an "enlarged system." This enlarged system now contains the open system and the collective degree of freedom, the reaction coordinate, extracted from the bath. The RC mapping can be used in conjunction with weak-coupling QME tools since, with a proper choice of parameters, the coupling of the *enlarged* system to the *residual* bath is weak. The RC method treats the system-reservoir coupling parameter *nonperturbatively* to obtain appropriate dynamical and steady-state properties of the original open system. The combined RC-QME approach has been utilized for studying the quantum dynamics of impurity models [13,86], thermal transport in nanojunctions [87–89], the operation of quantum thermal machines [19,20,90,91], transport in electronic systems [92–94], and problems of equilibration [13,95], as well as the dynamics of non-Markovian systems [96]. As useful as this tool has been in recent years and despite relying on an analytical mapping, in practice this approach has been only used as a numerical method due to the large Hilbert space of the enlarged system.

The polaron or Lang-Firsov transformation is central to many-body physics, with applications extending far beyond the original coupled electron-phonon problem. The concept of a polaron originates from solid-state physics, whereby lattice vibrations couple to the electron, generating a heavy electron with an effective mass representing the electron plus the phonon cloud surrounding it [97]. In the broader context of an impurity immersed in a harmonic bath, the polaron transformation allows us to unitarily map the system to the polaron frame where the system Hamiltonian is dressed by the system-bath coupling, making it amenable to perturbative treatments in the so-called nonadiabatic parameter (tunneling splitting). This approach has been used, e.g., to simulate heat transport through quantum nanojunctions [68,69,98,99] and later further extended using the polaron-transformed QME [73,74,100,101]. However, despite providing analytical insight into spin-boson–type models, the polaron mapping can become cumbersome, with compound (nonadditive) bath interaction terms. As such, it has mainly been utilized in simplified models with independent baths locally affecting the system (see, e.g., Refs. [102,103]) or by restricting the form of the system Hamiltonian to eliminate the formation of composite interaction terms [104].

In this work, we combine two central transformations in open-quantum-system methodologies, namely, the reaction-coordinate mapping and the polaron transformation, and develop a general and robust tool for *understanding* and *feasibly simulating* strong-coupling features in quantum transport and thermodynamics. Both of these transformations are applied onto harmonic degrees of freedom and as such, our focus is on strong coupling with harmonic baths. The essence of this newly developed reaction-coordinate polaron-transform (RCPT) approach is that the succession of these two transformations *imprints* strong-coupling effects *directly* into the system Hamiltonian, which after the transformations becomes *weakly* coupled to the (residual) surroundings, allowing the use of weak-coupling techniques. Furthermore, due to the additional truncation of the RC manifold, the dimensionality of the Hilbert space is identical to the starting one. Thus, the RCPT method allows us to *observe* the role of strong-coupling effects and *perform* numerical simulations that nonperturbatively handle strong-coupling effects *at the cost of a weak-coupling treatment*.

After introducing the RCPT method, rather than focusing on benchmarking it against numerically exact approaches, we exemplify the physics revealed by the formalism and predict signatures of strong coupling in several classes of open quantum systems. We apply the RCPT approach and tackle five central classes of problems encountered in quantum transport and quantum

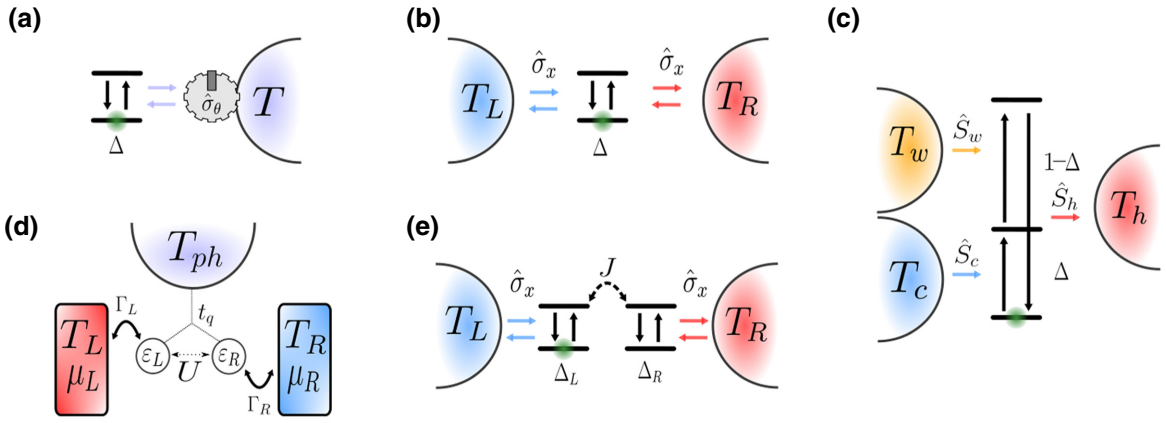

FIG. 1. Diagrams of the five problems examined in this work using the RCPT method. (a) *Quantum thermalization*, studied with a two-level impurity spin coupled to a bosonic reservoir experiencing both decohering and energy-exchange effects. (b) *Quantum heat transport*, examined on a minimal model of a spin system coupled to two bosonic reservoirs with a temperature bias. (c) *Quantum refrigeration*, examined on a three-level quantum absorption refrigerator, where each transition couples to a different reservoir, resulting in the net effect of extracting heat from the cold environment. (d) *Thermoelectric performance of nanojunctions*, illustrated on a phonon-assisted double-quantum-dot nanojunction. Here, charge is transported between the two leads with the help of a phonon environment. (e) *Dissipative spin chains*, with each spin coupled to an independent heat bath, here illustrated with a two-qubit model.

thermodynamics. Namely, we study strong system-bath coupling effects in (a) thermalization, (b) thermal energy transport, (c) refrigeration, (d) phonon-coupled electronic transport in the context of thermoelectric power generators, and (e) many-body, dissipative spin-lattice physics. Figure 1 illustrates these five models.

The paper is organized as follows. We present the RCPT theoretical framework in Sec. II. We exemplify the method on five key open-system problems and demonstrate that their behavior is greatly altered by strong system-bath coupling effects: quantum thermalization (Sec. III), steady-state heat transport (Sec. IV), quantum refrigeration (Sec. V), phonon-assisted charge transport in thermoelectric engines (Sec. VI), and steady-state dissipative spin-chain models (Sec. VII). In each section, theoretical predictions from the RCPT method are illustrated by numerical examples. We discuss and summarize our findings in Sec. VIII.

II. THE RCPT THEORETICAL FRAMEWORK

In this section, we describe the protocol for transforming an open-system Hamiltonian using the RCPT, thus arriving at what we refer to as an *effective Hamiltonian*, allowing for the interpretation of strong-coupling effects in open quantum systems at low cost. For simplicity, we present here the approach assuming a single heat bath; generalizations are discussed in Sec. II F. We work in units of $\hbar \equiv 1$, $k_B \equiv 1$, and $e \equiv 1$.

We consider a generic open-quantum-system model, with an impurity system coupled to a bosonic reservoir:

$$\hat{H} = \hat{H}_s + \sum_k \nu_k \left(\hat{c}_k^\dagger + \frac{t_k}{\nu_k}\hat{S}\right)\left(\hat{c}_k + \frac{t_k}{\nu_k}\hat{S}\right). \quad (1)$$

In this expression, $\hat{H}_s$ is the Hamiltonian of the system. $\hat{S}$ is a system operator and it couples to the displacement of reservoir modes of frequency ν_k with coupling strength t_k assumed to be a real number; k is a wave-vector index. Furthermore, $\hat{c}_k^\dagger$ ($\hat{c}_k$) are the bosonic creation (annihilation) operators for the bath modes. The interaction between the system and the reservoir is fully captured by the spectral density function, $J(\omega) = \sum_k t_k^2 \delta(\omega - \nu_k)$.

The framework consists of three steps, illustrated in Fig. 2.(i) An exact reaction-coordinate mapping is performed on the bosonic reservoir, identifying a central degree of freedom to be extracted from the reservoir and incorporated as part of the system. This creates an *extended* open system, which comprises the original system along with its coupled reaction-coordinate mode. This extended system is coupled to the residual bath with a modified spectral density function, typically with a weakened coupling strength compared to the original model given in Eq. (1). (ii) A polaron transformation is applied on the reaction coordinate. The transformation "imprints" features of the RC into the original system and partially decouples the RC from the system. This step further generates new *direct* interaction terms between the original system and the residual bath, which provides insight into the strong-coupling features of the model. Transformations (i) and (ii) are exact and unitary. (iii) The Hamiltonian is truncated assuming that only the ground state of the reaction coordinate is populated. This approximate step relies on the reaction-coordinate frequency (which derives from the spectral structure of the original bath) being the largest energy scale in the problem; notably, exceeding the thermal energy, which is our working assumption here. More details on the consequences of this approximation are included in Sec. II E.

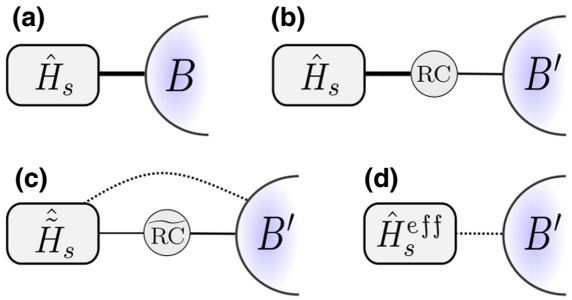

FIG. 2. A diagrammatic representation of the RCPT Hamiltonian transformations and truncation. (a) The original model: an open system ($\hat{H}_s$) coupled to a bosonic bath (B). (b) The system is extended to include a reaction coordinate, which is extracted from the reservoir, leaving a residual bath B' missing one mode. (c) The model after the application of the polaron transformation: the rotated system Hamiltonian connects to both the RC and the residual bath. (d) The model after the truncation of the RC, resulting in a so-called effective Hamiltonian with the system coupled only to the residual bath. This model is reminiscent of the original system in (a).

We refer to the application of these three steps in succession as the RCPT method. Once the RCPT procedure is performed, an effective Hamiltonian emerges, which mathematically resembles the original model given in Eq. (1). However, the parameters in the new effective model contain an explicit dependency on the original system-bath coupling parameters. This in turn allows for the interpretation of strong-coupling features. In what follows, we present this protocol to generate effective-Hamiltonian models as a means of capturing strong-coupling effects in open quantum systems.

A. Reaction-coordinate mapping

The first step in deriving effective-Hamiltonian models using the RCPT method is to perform an exact reaction-coordinate mapping [82] on the Hamiltonian in Eq. (1). This transformation results in the extraction of a collective reservoir mode of frequency Ω, which couples to the system at strength λ and is included as part of the system. We refer to the resulting Hamiltonian as the *reaction-coordinate Hamiltonian*,

$$\hat{H}_{\mathrm{RC}} = \hat{H}_s + \Omega\left(\hat{a}^\dagger + \frac{\lambda}{\Omega}\hat{S}\right)\left(\hat{a} + \frac{\lambda}{\Omega}\hat{S}\right) + \sum_k \omega_k \left(\hat{b}_k^\dagger + \frac{f_k}{\omega_k}(\hat{a}^\dagger + \hat{a})\right)\left(\hat{b}_k + \frac{f_k}{\omega_k}(\hat{a}^\dagger + \hat{a})\right), \tag{2}$$

where the reaction coordinate is defined such that

$$\lambda(\hat{a}^\dagger + \hat{a}) = \sum_k t_k(\hat{c}_k^\dagger + \hat{c}_k). \tag{3}$$

In the above expression, the bosonic creation (annihilation) operator of the RC is $\hat{a}^\dagger$ ($\hat{a}$) and it is coupled with strength f_k to the residual bath, identified by the creation (annihilation) bosonic operators $\hat{b}_k^\dagger$ ($\hat{b}_k$) of frequency ω_k. In the RC representation, the coupling parameter λ between the system and the reaction coordinate and the frequency of the reaction coordinate Ω are obtained from the original spectral density function via the expressions [82]

$$\lambda^2 = \frac{1}{\Omega}\int_0^\infty \omega J(\omega) d\omega \tag{4}$$

and

$$\Omega^2 = \frac{\int_0^\infty \omega^3 J(\omega) d\omega}{\int_0^\infty \omega J(\omega) d\omega}. \tag{5}$$

Note that λ characterizes the extent of interaction between the original system and the bath. As such, it is a central parameter to tune in the exploration of quantum dissipative behavior at strong coupling.

In the RC picture, a different spectral density function now characterizes the interaction between the RC and the residual bosonic environment, $J_{\mathrm{RC}}(\omega) = \sum_k f_k^2 \delta(\omega - \omega_k)$. From Heisenberg's equation of motion, it can be shown that this newly defined spectral density function is related to the original spectral density function by [82]

$$J_{\mathrm{RC}}(\omega) = \frac{2\pi\lambda^2 J(\omega)}{\left[P\int \frac{J(\omega')}{\omega'-\omega}d\omega'\right]^2 + \pi^2 J(\omega)^2}, \tag{6}$$

where in this expression, the integration is understood as a principal-value integral.

In the reaction-coordinate representation, the system-reservoir boundary is shifted to include an additional mode from the reservoir, resulting in an extended system, given by the first two terms of Eq. (2). The last term of Eq. (2) represents the residual environment and its interaction to the reaction coordinate.

The power of the RC transformation stems from the fact that when increasing the coupling strength, $J(\omega) \to \alpha J(\omega)$ with $\alpha > 0$, only the system reaction-coordinate coupling strength gets modified to $\lambda \to \sqrt{\alpha}\lambda$, while $J_{\mathrm{RC}}(\omega)$ does not change with α. This allows one to perform perturbative quantum master-equation calculations on the enlarged system, providing a valid strong-coupling treatment relying on weak-coupling tools.

B. Polaron transformation

In the second step of the RCPT method, we perform a polaron transformation on the reaction-coordinate Hamiltonian in Eq. (2). This unitary transformation is given by

the shift operator

$$\hat{U}_P = e^{(\lambda/\Omega)(\hat{a}^\dagger - \hat{a})\hat{S}}, \tag{7}$$

which partially decouples the system from the RC, as we explain below. As a consequence of this transformation, we generate new *direct* coupling terms between the residual bath and the system as well as the RC and the system. We note that our polaron operator lives in the Hilbert space of the system and the RC.

To perform the transformation, we rely on the fact that $\hat{U}_P \hat{a} \hat{U}_P^\dagger = \hat{a} - (\lambda/\Omega)\hat{S}$ and we use the shorthand notation for the polaron-transformed reaction-coordinate system Hamiltonian $\hat{\tilde{H}}_s \equiv \hat{U}_P \hat{H}_s \hat{U}_P^\dagger$. The total polaron-transformed reaction-coordinate Hamiltonian is $\hat{H}_{\mathrm{RC-P}} \equiv \hat{U}_P \hat{H}_{\mathrm{RC}} \hat{U}_P^\dagger$, given by

$$\begin{aligned}\hat{H}_{\mathrm{RC-P}} = \hat{\tilde{H}}_s + \Omega \hat{a}^\dagger \hat{a} \\ + \sum_k \omega_k \left\{ \left[\hat{b}_k^\dagger + \frac{f_k}{\omega_k} \left(\hat{a}^\dagger + \hat{a} - \frac{2\lambda}{\Omega} \hat{S} \right) \right] \right. \\ \left. \times \left[\hat{b}_k + \frac{f_k}{\omega_k} \left(\hat{a}^\dagger + \hat{a} - \frac{2\lambda}{\Omega} \hat{S} \right) \right] \right\}. \end{aligned} \tag{8}$$

Since the system Hamiltonian is dressed by the polaron-transformation operator, it is now a function of the system-bath coupling parameter λ. Another way to think about this is that the transformation "imprints" the RC into the system Hamiltonian. Furthermore, new interaction terms emerge in the polaron frame. Namely, the system now couples *directly* to both the RC ($\hat{a}$ operators) and to the residual bath ($\hat{b}_k$ operators). However, the functional form of the spectral density function of the residual bath is unaltered by this transformation and it is still captured by Eq. (6), albeit with an additional prefactor $(2\lambda/\Omega)^2$.

At first glance, applying the polaron operator after the RC transformation seems unconducive for performing calculations, as there are now terms coupling the system to both the RC and the residual environment. In fact, we appear to have made the Hamiltonian more complex to solve due to the appearance of new interaction terms. As we show next, the Hamiltonian in Eq. (8) is actually an intermediate step in deriving effective-Hamiltonian models and after an additional simplifying approximation, it becomes tractable.

C. Reaction-coordinate truncation

The RC and the polaron transformations are exact. As such, no approximations are made up to this point. To simplify the Hamiltonian in Eq. (8), we now invoke an approximation, generating an *effective Hamiltonian* $\hat{H}^{\mathrm{eff}}(\lambda)$. This effective Hamiltonian is transparent for analytical work and it also serves as a good starting point for numerical implementations.

Assuming Ω, the frequency of the RC, to be the largest energy scale in the problem (see a discussion in Sec. II E)—higher, in particular, than the temperature of the attached bath(s), $\Omega \gg T$—one can safely truncate the harmonic manifold of the RC and consider only its ground level. The truncation does not eliminate strong-coupling effects in a regime where Ω is the largest energy scale.

We thus define the effective Hamiltonian as the subspace of Eq. (8) in which the RC is fixed to its ground state $|0\rangle$:

$$\hat{H}^{\mathrm{eff}}(\lambda) = \langle 0 | \hat{H}_{\mathrm{RC-P}} | 0 \rangle. \tag{9}$$

Explicitly,

$$\hat{H}^{\mathrm{eff}}(\lambda) = \langle 0 | \hat{\tilde{H}}_s | 0 \rangle + \sum_k \omega_k \left(\hat{b}_k^\dagger - \frac{2\lambda f_k}{\Omega \omega_k} \hat{S} \right) \left(\hat{b}_k - \frac{2\lambda f_k}{\Omega \omega_k} \hat{S} \right). \tag{10}$$

We highlight here the dependency of the effective system Hamiltonian on the coupling parameter λ; however, the effective model also depends on additional system parameters, such as the RC frequency, Ω.

Crucially, the effective Hamiltonian in Eq. (10) has a mathematical structure similar to the original Hamiltonian in Eq. (1). Two important distinctions are, however, apparent. (i) The system Hamiltonian is dressed by the polaron-transformation operator,

$$\hat{H}_s^{\mathrm{eff}}(\lambda) = \langle 0 | \hat{\tilde{H}}_s | 0 \rangle. \tag{11}$$

(ii) The reservoir considered here is the residual bath that is obtained in the RC mapping [see Eq. (2)]. The spectral density function of the bath is further dressed by the RC parameters:

$$J^{\mathrm{eff}}(\omega) = \frac{4\lambda^2}{\Omega^2} J_{\mathrm{RC}}(\omega). \tag{12}$$

This completes the introduction of the RCPT method. Considering a general Hamiltonian strongly coupled to a bath [see Eq. (1)], we map the model into Eq. (10), with a λ-dressed system Hamiltonian and a *weak* system-bath coupling. This is because $J_{\mathrm{RC}}(\omega)$ describes the coupling of the extended system to a residual bath, which is by construction weakened relative to the original case. Also, we further assume that $\lambda/\Omega \ll 1$ for Ω to retain its status as the largest energy scale in the problem.

The RCPT method allows nonpertubative studies of strong-coupling models. The elegant and powerful aspects of the RCPT method stem from the effective Hamiltonian in Eq. (10) seemingly having the same complexity as the original model. This in turn allows the effective Hamiltonian to be treated with weak-coupling methods, since the

original system-bath coupling energy λ is quenched and absorbed into redefining the system itself. The main novelty of the method lies in it allowing analytical studies of the strong-coupling regime. Since at weak coupling one can often approach the problem analytically and acquire closed-form expressions for, e.g., nonequilibrium steady-state properties, one can now build on these solutions—but with renormalized parameters and a dressed system Hamiltonian. Moreover, even without performing a detailed analysis, the form of the Hamiltonian in Eq. (10), compared to Eq. (1), immediately exposes contributions of strong coupling to the open quantum system, e.g., in opening new transport pathways and shifting parameters.

We now go one step further and manipulate the effective system Hamiltonian to cast it in a more transparent form, which will be useful in applications:

$$\hat{H}_s^{\mathrm{eff}}(\lambda) = \langle 0|e^{(\lambda/\Omega)(\hat{a}^\dagger - \hat{a})\hat{S}}\hat{H}_s e^{-(\lambda/\Omega)(\hat{a}^\dagger - \hat{a})\hat{S}}|0\rangle. \tag{13}$$

The polaron operators are mathematically analogous to displacement operators encountered in quantum optics. They have the useful property of generating coherent states when acting on the vacuum $D(\alpha)|0\rangle = |\alpha\rangle$. Furthermore, coherent states may be written as a superposition of harmonic oscillator eigenstates. We employ these two properties defining $\alpha \equiv (\lambda/\Omega)\hat{S}$ as an operator. This results in a useful form for the effective system Hamiltonian:

$$\hat{H}_s^{\mathrm{eff}}(\lambda) = e^{-(\lambda^2/2\Omega^2)\hat{S}^2}\left(\sum_{n=0}^{\infty}\frac{\lambda^{2n}}{\Omega^{2n}n!}\hat{S}^n\hat{H}_s\hat{S}^n\right)e^{-(\lambda^2/2\Omega^2)\hat{S}^2}. \tag{14}$$

This expression allows for the computation of the effective system Hamiltonian, which is now coupling-strength dependent. Further details are given in Appendix A.

The effective Hamiltonian in Eq. (10) concludes the theoretical account of the RCPT framework. In Sec. II D, we summarize the evolution of the spectral density function during the RCPT steps. We discuss the assumptions of the RCPT method and thus its regime of validity in Sec. II E. Theoretical extensions to the basic framework are presented in Sec. II F. The numerical QME implementation of the method to study transport behavior is described in Sec. II G.

D. Evolution of the spectral density function in the RCPT method

The RCPT method is not limited to a specific type of spectral density function and the procedure outlined above is general. However, to make the method useful, one should work in a parameter range such that, although the original model may carry strong couplings to the bath, $J_{\mathrm{RC}}(\omega)$ corresponds to a weak-coupling situation. In this work, we exemplify the RCPT method using the Brownian spectral density function,

$$J(\omega) = \frac{4\gamma\Omega^2\lambda^2\omega}{(\omega^2-\Omega^2)^2 + (2\pi\gamma\Omega\omega)^2}. \tag{15}$$

In this model, the coupling of the system to the bath is peaked at Ω with a width parameter γ. λ tunes the system-reservoir coupling strength. It can be shown [13,86,87] that performing a reaction-coordinate mapping, via Eq. (6), translates this spectral density function to an Ohmic form,

$$J_{\mathrm{RC}}(\omega) = \gamma\omega e^{-|\omega|/\Lambda}. \tag{16}$$

This expression becomes exact when Λ, the cutoff energy, tends to infinity. In the RC representation, the dimensionless width parameter γ controls the coupling strength between the RC and the residual environment. Furthermore, in this model the location of the central peak, Ω, maps to the frequency of the reaction coordinate. Thus, a narrow Brownian function translates to an extended system weakly coupled to the residual bath.

After the polaron transformation, we build the effective model and the spectral density function is further dressed according to Eq. (12), ending with

$$J^{\mathrm{eff}}(\omega) = \frac{4\lambda^2}{\Omega^2}\times\gamma\omega e^{-|\omega|/\Lambda}. \tag{17}$$

This spectral density function increases with λ, unlike $J_{\mathrm{RC}}(\omega)$, which does not vary with the coupling strength, as discussed below Eq. (6). However, the coupling to the bath is ensured to be weak based on the dimensionless width parameter γ, which should be made small. Furthermore, the RCPT method relies on $\lambda < \Omega$; thus the coupling strength of the effective model to the heat bath remains weak, supporting the perturbative system-bath treatment. Nevertheless, in simulations performed below, we explore the behavior pushing parameters from weak coupling to the regime of $\lambda/\Omega \sim 1$, yet we achieve reasonable results with the RCPT method, compared to other techniques. This pleasing success arises for two reasons. (i) We employ γ that is small enough, justifying a weak-coupling treatment irrespective of the ratio λ/Ω. (ii) In the models studied here, we find that λ-renormalized level splittings are still significantly smaller than the RC frequency Ω, such that the RCPT truncation remains credible even in the ultrastrong-coupling regime.

In what follows, we describe bosonic baths using the Brownian spectral density function. In contrast, we treat fermionic reservoirs under the weak system-reservoir coupling assumption and take them in the wide-band limit.

E. Regimes of applicability of the RCPT formalism

In this section, we discuss the only approximation of the RCPT mapping: representing the manifold of the RC

solely by its ground state. We first identify the parameter regime where this approximation holds. We then discuss the types of problems that would benefit from being addressed by the RCPT technique. We emphasize that once the RCPT mapping is complete and we reach the effective Hamiltonian in Eq. (10), different analytical and numerical tools can be implemented on the effective Hamiltonian. These tools may come with their own independent sets of approximations; in this section, however, we focus exclusively on the approximation of the RCPT mapping.

Considering an open-quantum-system model, we list the relevant energy scales in the problem: Δ would serve as a characteristic energy scale for the system, e.g., spin splitting in a spin-bath model; Ω is a characteristic frequency for the bath; λ characterizes the system-bath coupling; and T is the thermal energy.

Let us now discuss the energy spectrum of the RC Hamiltonian. For a large value of Ω relative to the eigenspectrum of the bare system and the coupling energy, $\Omega \gg \Delta, \lambda$, the energy spectrum of Eq. (2) shows manifolds of levels separated by gaps of $\mathcal{O}(\Omega)$. In each manifold, the levels roughly correspond to the original system thus they are spaced by $\mathcal{O}(\Delta)$. For example, for a two-level system with splitting $\Delta \ll \Omega$ and coupling strength to the bath $\lambda \ll \Omega$, the eigenspectrum of the system plus RC [see Eq. (2)] includes manifolds roughly separated by Ω, each with a pair of states; the lowest manifold corresponds to the RC in its ground state while the spin of the system occupies either its ground or excited states. Higher manifolds correspond to excited RCs, again with the spin of the system residing in two possible states (see also Ref. [87]). It is important to note that there is no restriction on the relative magnitude of λ and Δ. Furthermore, in the examples studied in this paper, we find that even at very strong λ (of the order of Ω), the picture of manifolds described here remains largely valid, making the truncation of the RC physical even in the ultrastrong-coupling regime. In general, one should examine (numerically or analytically) the λ dependence of the eigenvalues of the extended system [Eq. (2)]. This would allow identification of the range of λ over which the truncation of the RC (or, similarly, the RC $-$ P) Hamiltonian can be physically motivated. The truncation of the RC performed in Sec. II C is justified as long as $\Omega \gg T$. In this regime, the thermal energy from the bath is insufficient to significantly populate higher excited states of the reaction coordinate.

Altogether, on a rigorous ground, the RCPT formalism presented in this work is expected to be valid when $\Omega \gg \Delta, \lambda$ and $\Omega \gg T$. In practice, however, for a broad range of models, the requirement $\Omega \gg \lambda$ can be relaxed, since λ only mildly shifts the bare levels relative to Ω, even in the ultrastrong regime. Note that there is no limitation on whether the thermal energy is higher or lower than the characteristic energies in the system, Δ. In impurity models, the temperature is defined low or high relative to the eigenvalues of the system Hamiltonian. Therefore, the RCPT procedure is valid for both high and low temperatures.

What types of problems would benefit from being represented with the effective Hamiltonian? The truncation of the RC to its ground state accurately captures the impact of strong coupling in transport phenomena, as we show in the following sections. However, the truncation drastically curtails the ability to follow dynamical effects, as we now explain. The reaction-coordinate method captures non-Markovian dynamics (see, e.g., Refs. [13,96]). This is possible because of the build-up of correlations during time evolution between the system and the RC (which, in truth, is part of the bath). An undesired consequence of the RC truncation is losing this ability to exchange information between the RC and the system and, hence, missing dynamical features that emerge due to non-Markovianity. In other words, in the RCPT formalism, the RC does not evolve in time; it is maintained in its ground state. As a result, transient features in the dynamics, e.g., some oscillations, would be missed. However, the RCPT method recovers the correct decay constants at strong couplings; thus the steady-state limit is well described.

The RCPT method can be systematically made more accurate by keeping higher excited states of the RC. This approach, described in Appendix B, would recover missing dynamical features. However, this is achieved at the cost of exponentially increasing the dimensionality of the Hilbert space of the system, thus losing insights gained from the elegant effective-Hamiltonian picture.

F. Extensions

1. Iterative mapping

In implementing the RCPT method on Eq. (1), we arrive at a form that closely resembles the initial Hamiltonian, except with a λ-dressed effective system Hamiltonian and a different spectral density function. In principle, it should be possible to iterate this process: repeatedly extract an RC mode from the bath, perform a polaron transformation on this mode, and truncate the RC to only occupy its ground state. This process would lead to an effective description including strong-coupling effects even with highly structured spectral density functions, e.g., a bimodal function. The effective Hamiltonian after n such rounds (where n is still significantly smaller than the number of modes in the bath) would have the following structure:

$$\hat{H}_n^{\mathrm{eff}} = \langle \mathbf{0}_n | \hat{\tilde{H}}_s^{(n)} | \mathbf{0}_n \rangle + \sum_k \omega_k \left\{ \left[\hat{b}_k^\dagger + \prod_{i=1}^{n} \left((-1)^i \frac{2\lambda_i}{\Omega_i} \right) \frac{f_k}{\omega_k} \hat{S} \right] \times \left[\hat{b}_k + \prod_{i=1}^{n} \left((-1)^i \frac{2\lambda_i}{\Omega_i} \right) \frac{f_k}{\omega_k} \hat{S} \right] \right\}. \quad (18)$$

In this expression, we use a shorthand notation to express the effective system Hamiltonian,

$$\langle \mathbf{0}_n|\hat{\tilde{H}}_s^{(n)}|\mathbf{0}_n\rangle \equiv \langle 0_1,\ldots,0_n|\prod_{i=1}^{n}(\hat{U}_{P,i})\hat{H}_s\prod_{i=1}^{n}(\hat{U}_{P,i}^{\dagger})|0_1,\ldots,0_n\rangle, \tag{19}$$

where $|0_n\rangle$ denotes the ground state of the nth RC. The evaluation of this term is in fact simple, since the sequence of polaron transformations commutes. Additionally, the spectral density functions can be iteratively computed using Eq. (6) with w_k as the frequency of the bath modes after the last iteration, and f_k the coupling energies of those modes to the system. It is therefore straightforward to iterate this process as desired. We emphasize that even without iterating, that is, following the procedure given in Secs. II A–II C, the Hamiltonian includes strong-coupling effects in a nonperturbative manner.

2. Multibath problems

Another extension of interest concerns the application of this tool to study open quantum systems coupled to multiple environments. It is straightforward to extract simultaneously more than one RC, e.g., one from each bath. However, the polaron transform can become quite complicated when the extended model includes more than one RC. Namely, it is not guaranteed that the individual polaron transformations on each RC will commute with one another and this aspect depends on the details of the model. As such, we are left with the arbitrary freedom of deciding which polaron transform to apply first, potentially changing the outcome of the calculation (a fact that is not surprising, as this is not an exact tool). Given this nonuniqueness of the procedure, one would need to test different sequences of the polaron transformation and select the most feasible and tractable approach.

In summary, the RCPT approach is straightforward to apply in situations in which the system operators that couple to the different baths commute or if one applies only a single polaron transformation before truncating the reaction coordinate.

G. Numerical implementation: Redfield QME

Before tackling examples of impurity models with the RCPT method, we briefly review the numerical approach used in this work to simulate the steady-state limit of the reduced system dynamics, as well as different currents. We first emphasize that one should decouple the challenge of deriving an effective Hamiltonian, which by structure already reveals important physics, to the adopted simulation method. The simulation approach could be rather primitive, such as the Redfield QME (since strong-coupling effects are already embedded in the model Hamiltonian), or sophisticated, such as path-integral numerically exact tools, in which case the effective model likely offers an advantageous starting point to convergence.

Here, for simplicity, we implement the Redfield quantum master equation (QME), which relies on weak-coupling and Markov approximations, and simulate the nonequilibrium behavior of three Hamiltonians:

(i) the original model, given in Eq. (1)
(ii) the reaction-coordinate Hamiltonian in Eq. (2)
(iii) the effective Hamiltonian in Eq. (10), which constitutes the last step of the RCPT method

We emphasize that in all cases, we use the Born-Markov-Redfield (BMR) quantum master equation, which in case (ii) is performed on the extended system and in case (iii) on the effective model. In both of these cases, this second-order method is able to capture strong-coupling effects. In contrast, in case (i), the BMR-QME approach provides meaningful results only if the coupling strength in the original picture is weak. We first discuss the general Redfield equation and then comment on the modifications required to study each variation, cases (i), (ii), and (iii). Working in the Schrödinger representation and in the energy basis of the system Hamiltonian, the Redfield equation for the reduced density matrix $\rho(t)$ of the system is given by

$$\begin{aligned}\dot{\rho}_{mn}(t) = &-i\omega_{mn}\rho_{mn}(t)\\ &-\sum_{j,p}[R_{mj,jp}(\omega_{pj})\rho_{pn}(t) + R^{*}_{np,pj}(\omega_{jp})\rho_{mj}(t)\\ &- R_{pn,mj}(\omega_{jm})\rho_{jp}(t) - R^{*}_{jm,np}(\omega_{pn})\rho_{jp}(t)].\end{aligned} \tag{20}$$

The indices m (as well as n, j, and p) denote eigenstates of the system with eigenvalues E_m and Bohr frequencies $\omega_{mn} \equiv E_m - E_n$. The elements of the R superoperator are given by a half Fourier transform of the bath autocorrelation functions,

$$\begin{aligned}R_{mn,jp}(\omega) &= (S^D)_{mn}(S^D)_{jp}\int_0^{\infty} d\tau e^{i\omega\tau}\langle\hat{B}(\tau)\hat{B}(0)\rangle\\ &= (S^D)_{mn}(S^D)_{jp}[\Gamma(\omega) + i\Delta(\omega)],\end{aligned} \tag{21}$$

where $\hat{S}^D$ denotes the system operator that is coupled to the bath, written in the energy basis of the system Hamiltonian. Furthermore, $\Gamma(\omega)$ and $\Delta(\omega)$ are the real and imaginary parts of the bath autocorrelation function, respectively. These correlation functions are evaluated with respect to

the thermal state of the bath. In this work, we neglect the imaginary part of the autocorrelation function, as it contributes only a small shift to the spectrum.

For harmonic environments and a bilinear system-bath coupling, the real part of the R tensor evaluates to

$$\Gamma(\omega) = \begin{cases} \pi J(|\omega|)n(|\omega|), & \omega < 0, \\ \pi J(\omega)[n(\omega)+1], & \omega > 0, \\ \pi \lim_{\omega\to 0} J(\omega)n(\omega), & \omega = 0. \end{cases} \tag{22}$$

Here, $n(\omega)$ is the Bose-Einstein distribution function of the bath, characterized by an inverse temperature $\beta = 1/T$. In a compact form, the evolution of the system density matrix is given by

$$\dot{\rho}(t) = -i[\hat{H}_s, \rho(t)] + \sum_\alpha D_\alpha(\rho(t)), \tag{23}$$

where we already generalize the equation to include multiple thermal reservoirs with the dissipators $D_\alpha(\rho(t))$, organized based on Eq. (20).

We solve the equation of motion in the steady state and obtain the density matrix of the system, $\rho^{\rm SS}$. This can be achieved in different ways; here, we write down the equation of motion in a compact form as $\dot{\rho}(t) = \mathcal{L}\rho(t)$ and we further construct a modified Liouvillian $\mathcal{L}'$ by replacing the last row with a population- (probability-) conservation condition. We also define the column vector v with all its elements set to zero besides the last one, which corresponds to the population conservation condition with the diagonal elements of the density matrix of the system summing up to unity. The steady-state limit of the density matrix of the system is then obtained by algebraic operations,

$$\mathcal{L}'\rho^{\rm SS} = v. \tag{24}$$

This formalism allows the calculation of currents; e.g., the heat current at the αth contact is calculated from the heat exchanged between the system and the αth reservoir,

$$j_q^\alpha(t) = {\rm Tr}_s\left[D_\alpha(\rho(t))\hat{H}_s\right], \tag{25}$$

where steady-state currents are obtained once the state of the system in the long-time limit, $\rho^{\rm SS}$, is obtained. The heat current is defined to be positive when flowing from the αth bath toward the system. Similarly, the charge current at the αth contact is

$$j_e^\alpha(t) = {\rm Tr}_s\left[D_\alpha(\rho(t))\hat{N}_s\right], \tag{26}$$

where $\hat{N}_s$ is the number operator for the system.

We now elaborate on the three implementations of the Redfield QME that we use in this work:

(i) BMR-QME simulations refer to using the Born-Markov-Redfield quantum master equation directly on the original Hamiltonian in Eq. (1), with the associated spectral density function of the heat bath, given here in Eq. (15). The BMR QME provides inaccurate results in the strong system-bath coupling regime, as the method is stretched beyond its regime of validity. In this sense, we regard the BMR QME as an asymptotic solution of the weak-coupling limit.

(ii) RC-QME simulations refer to using the Redfield QME to study the extended system after adding the RC [see Eq. (2)] with the relevant spectral density function, here Eq. (16) [or, more generally, Eq. (6)]. In practice, we truncate the RC harmonic oscillator manifold, reducing it to its first M levels. The coefficients $(S^D)_{mn}$ in the dissipator [see Eq. (21)] are dictated by the form of the RC coupling to the bath [see the third term in Eq. (2)]. While the original system may be strongly coupled to the bath, in the RC representation the assumption of a weak coupling between the *residual* reservoir and the *extended* system can be justified as explained in Sec. II D.

(iii) EFF-QME simulations correspond to using the Redfield QME, except that we now apply it on the effective Hamiltonian in Eq. (10) with the spectral density function Eq. (12) [see also Eq. (17)]. Recall that the effective Hamiltonian is constructed with the RCPT framework. This approach allows for strong-coupling effects to be captured through renormalized parameters, while still retaining a simple and tractable quantum master-equation framework; the dimension of the Hilbert space of the effective system is equal to that of the original model. This approach is, in principle, less accurate than the RC QME since the RC manifold is truncated. However, the EFF-QME method should reliably capture predictions of the RC QME in the limit where Ω is the largest energy scale (for a discussion on this point, see Sec. II E).

The hierarchy of methods goes as follows. The RC QME provides the most accurate results at strong coupling, maintaining dynamical effects in the RC. However, it is a numerical method and it does not offer deep insights into the physical mechanisms of strong coupling. The EFF-QME method preserves dominant strong-coupling effects but is less accurate. On the other hand, it can provide a profound understanding of the underlying strong-coupling effects. The BMR QME is valid only at weak system-bath coupling.

In what follows, we study and simulate several prominent impurity models with the BMR-QME, RC-QME, and EFF-QME methods to illustrate the predictive power

of the RCPT approach. Our main argument, however, is that the effective Hamiltonian itself—namely Eq. (10), the outcome of the RCPT approach—already allows assessment of contributions of strong coupling to transport characteristics, even *without* performing simulations.

III. THERMALIZATION: WEAK-, INTERMEDIATE-, AND ULTRASTRONG-COUPLING LIMIT

What is the equilibrium state of a system that is coupled to a heat bath at temperature T? For macroscopic objects, statistical physics asserts that in the long-time (steady-state) limit, the system should reach the conventional Gibbs state, $\rho^{\rm SS} = (1/Z)e^{-\beta\hat{H}_s}$, where $\hat{H}_s$ is the Hamiltonian of the system, β is the inverse temperature of the bath, and $Z = {\rm Tr}_s\left[e^{-\beta\hat{H}_s}\right]$ is the relevant partition function, with the trace performed over the degrees of freedom of the system. However, the Gibbs-state assumption is valid only if the interaction of the system with the heat bath is vanishingly weak; it breaks down, e.g., for nanoscale systems once the interaction energy becomes comparable to the energy parameters of the system. The derivation of the equilibrium state as a function of the system-bath interaction energy has been a topic of recent focus, particularly when steady-state coherences are generated [22–27,30]. Note that in this section, the system is coupled to a single heat bath and we thus refer to the equilibrium state as the steady state. In the following sections, when dealing with multiple heat baths, the steady state is a nonequilibrium state.

What, then, is the long-time state of a quantum system coupled to a heat bath? The general statement is that the system should reach the mean-force Gibbs state (MFGS), defined as

$$\rho^{\rm SS}_{\rm MFGS} = \frac{1}{Z_{\rm MFGS}}{\rm Tr}_B\left[e^{-\beta\hat{H}}\right], \tag{27}$$

which is the state obtained once taking a partial trace over the degrees of freedom of the bath. Here, $\hat{H}$ is the total Hamiltonian and the partition function is defined with the full trace, $Z_{\rm MFGS} = {\rm Tr}[e^{-\beta\hat{H}}]$. Generally, this MFGS *differs* from the conventional Gibbs state. An analytical expression for the MFGS has been obtained for the Caldeira-Leggett model in the ultrastrong-coupling limit [26,30]. It has been shown that in this case, the equilibrium state of the system is diagonal—albeit in the basis of the system operator that couples to the bath.

Here, we show that the effective model, the outcome of the RCPT process, provides an excellent *analytical* approximation for the MFGS from weak coupling, through the intermediate regime, to the ultrastrong-coupling limit. In fact, in Appendix C, we show that in the ultrastrong limit, the RCPT method builds the exact MFGS as derived in Ref. [26]. Here, we perform this analysis on the generalized spin-boson model with a spin coupled to a harmonic reservoir,

$$\hat{H} = \Delta\hat{\sigma}_z + \sum_k \nu_k\left(\hat{c}_k^\dagger + \frac{t_k}{\nu_k}\hat{\sigma}_\theta\right)\left(\hat{c}_k + \frac{t_k}{\nu_k}\hat{\sigma}_\theta\right), \tag{28}$$

where Δ is the spin splitting. The spin is coupled to a bosonic bath with parameters as defined in Eq. (1). The system interaction operator to the bath is $\hat{\sigma}_\theta = \cos(\theta)\hat{\sigma}_z + \sin(\theta)\hat{\sigma}_x$, where $0 \le \theta \le \pi/2$ is the angle of a vector pointing in the x-z plane of the Bloch sphere, determining the nature of the system-bath interaction. With this definition, $\theta = \pi/2$ corresponds to the standard spin-boson model, while $\theta = 0$ is the pure dephasing model, where only decoherence dynamics are observed. In the language of Eq. (1), the generalized spin-boson model Eq. (28) corresponds to the choice $\hat{H}_s = \Delta\hat{\sigma}_z$ and $\hat{S} = \hat{\sigma}_\theta$.

On the basis of Eqs. (10)–(14), we write down directly the effective Hamiltonian obtained from Eq. (28) through the RCPT procedure. Making use of the properties of the Pauli operators we get $\hat{S}^2 = 1$ and $\hat{S}^3 = \hat{S}$, we break down the sum in Eq. (14) into even and odd contributions:

$$\hat{H}_s^{\rm eff}(\lambda) = e^{-(\lambda^2/\Omega^2)}\left(\sum_{n;{\rm even}}\frac{\lambda^{2n}}{\Omega^{2n}n!}\hat{H}_s + \sum_{n;{\rm odd}}\frac{\lambda^{2n}}{\Omega^{2n}n!}\hat{S}\hat{H}_s\hat{S}\right). \tag{29}$$

We sum the series noting that $\hat{S}\hat{H}_s\hat{S} = \Delta\sin(2\theta)\hat{\sigma}_x + \Delta\cos(2\theta)\hat{\sigma}_z$. The effective system Hamiltonian thus becomes

$$\hat{H}_s^{\rm eff}(\lambda) = e^{-(\lambda^2/\Omega^2)}\cosh\left(\frac{\lambda^2}{\Omega^2}\right)\Delta\hat{\sigma}_z + e^{-(\lambda^2/\Omega^2)}\left[\sinh\left(\frac{\lambda^2}{\Omega^2}\right)(\Delta\sin(2\theta)\hat{\sigma}_x + \Delta\cos(2\theta)\hat{\sigma}_z)\right]. \tag{30}$$

Next, we rearrange this expression into the form

$$\hat{H}_s^{\rm eff}(\lambda) = \frac{\Delta}{2}\left[(1 + e^{-(2\lambda^2/\Omega^2)}) + (1 - e^{-(2\lambda^2/\Omega^2)})\cos(2\theta)\right]\hat{\sigma}_z + \frac{\Delta}{2}\left(1 - e^{-(2\lambda^2/\Omega^2)}\right)\sin(2\theta)\hat{\sigma}_x. \tag{31}$$

This is the effective Hamiltonian for the system and it uncovers two important aspects of strong coupling. (i) Parameter renormalization: as can be seen from the first row in Eq. (31), the qubit splitting is suppressed when $\theta \neq 0$ once $\lambda > 0$, since $\frac{1}{2}\left[(1+e^{-(2\lambda^2/\Omega^2)})+(1-e^{-(2\lambda^2/\Omega^2)})\cos(2\theta)\right] \leq 1$. (ii) Generation of new processes: the second row in Eq. (31) reveals that a new system-tunneling term appears for $0 < \theta < \pi/2$, compared to the original Hamiltonian in Eq. (28). This term is being induced by the system-bath coupling, $\lambda \neq 0$. To gain insight into the strong-coupling features of this model, we consider three angles as special cases:

(1) The pure-dephasing model is realized when $\theta = 0$. This reduces Eq. (31) to

$$\hat{H}_s^{\text{eff}}(\lambda, \theta = 0) = \Delta\hat{\sigma}_z. \tag{32}$$

In this case, $[\hat{H}_s, \hat{S}] = 0$,and therefore the polaron shift operator commutes with the system Hamiltonian. As a result, the system Hamiltonian is unchanged by the RCPT procedure.

(2) The standard spin-boson model is obtained when $\theta = \pi/2$:

$$\hat{H}_s^{\text{eff}}(\lambda, \theta = \pi/2) = \Delta e^{-(2\lambda^2/\Omega^2)}\hat{\sigma}_z. \tag{33}$$

Here, the spin-splitting is *exponentially* suppressed due to the coupling to the environment but no new terms (processes) are generated in the system Hamiltonian. This observation clearly points to the nonperturbative nature of the RCPT scheme.

(3) The intermediate angle $\theta = \pi/4$ leads to

$$\hat{H}_s^{\text{eff}}(\lambda, \theta = \pi/4) = \frac{\Delta}{2}(1+e^{-(2\lambda^2/\Omega^2)})\hat{\sigma}_z + \frac{\Delta}{2}(1-e^{-(2\lambda^2/\Omega^2)})\hat{\sigma}_x. \tag{34}$$

This intermediate case reveals the general features of strong coupling as predicted by this technique: the qubit frequency is renormalized, similar to the standard spin-boson model, and a new tunneling term is generated.

A. Spectrum of the spin-boson model

To showcase the predictive power of the RCPT method, we next compare the eigenenergy spectrum of the extended RC system, which is formally exact and is obtained from simulations, with the eigenenergies of the effective system Hamiltonian, which are inexact but are given by analytical expressions. Our results are displayed in Figures 3(a)–3(c) for the three different angles $\theta = \pi/2$, $\theta = 0$, and $\theta = \pi/4$, respectively.

We diagonalize Eq. (31) and find the effective spin splitting for the three angles:

$$\Delta_{\text{eff}}(\lambda, \theta = 0) = \Delta, \tag{35}$$

$$\Delta_{\text{eff}}(\lambda, \theta = \pi/2) = \Delta e^{-(2\lambda^2/\Omega^2)}, \tag{36}$$

$$\Delta_{\text{eff}}(\lambda, \theta = \pi/4) = \frac{\Delta}{\sqrt{2}}\sqrt{1+e^{-(4\lambda^2/\Omega^2)}}. \tag{37}$$

In parallel, using the RC Hamiltonian, we study the energy spectrum of the extended system Hamiltonian, the first line of Eq. (2). We focus on the gap between the first excited state and the ground state. In Fig. 3, we show that this gap is perfectly reproduced by the energy differences of the effective Hamiltonian, as written in Eqs. (35)–(37). This agreement holds, surprisingly, even at very strong coupling with $\lambda > \Omega$. We conclude that the RCPT technique provides an excellent approximation for the lowest energy levels of the system Hamiltonian, with strong-coupling effects absorbed in their definitions. More broadly, as we show next, the method brings an intuition on the expected impact of strong-coupling effects in open-system phenomena.

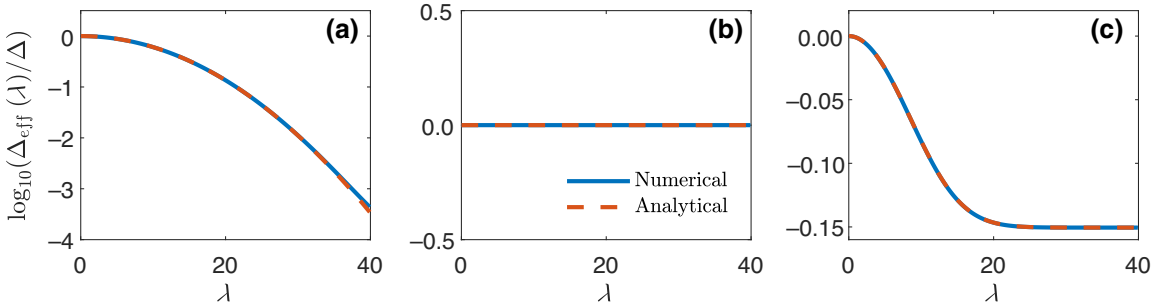

FIG. 3. The spectrum of the generalized spin boson model. We display $\Delta_{\text{eff}}(\lambda)$, the energy gap between the first-excited-state and ground-state eigenenergies of the spin system as a function of the system-bath coupling for three different angles: (a) $\theta = \pi/2$, (b) $\theta = 0$, and (c) $\theta = \pi/4$. Analytical expressions obtained from the effective spin splittings [see Eqs. (35)–(37)] (dashed lines) agree perfectly with results from the numerical diagonalization of Eq. (2), applied to the generalized spin-boson model (solid lines). The parameters used here are $\Delta = 1$ and $\Omega = 20$.

B. Thermalization in the spin-boson model

We now examine the long-time steady-state value of the density matrix of the system as a function of the system-reservoir coupling parameter, λ. Our main achievement here is the derivation of a closed-form analytical expression for the steady state of the system, [Eq. (40) and Eq. (C9) in Appendix C], which is *exact* in both the weak and ultrastrong-coupling limits. Moreover, it provides an excellent qualitative approximation to the steady state in the intermediate-coupling regime.

In Figs. 4(a) and 4(b), we present the population of the excited state and the magnitude of the coherences of the spin, respectively, in the eigenbasis of the system Hamiltonian for $\theta = \pi/4$ using $\Omega = 20$. We present the elements of the density matrix using different methods:

(i) The ultraweak steady state (UW) corresponds to the conventional Gibbs state,

$$\rho^{\rm SS}_{\rm UW} = \frac{1}{Z_{\rm UW}} e^{-\beta \hat{H}_s}, \tag{38}$$

where $Z_{\rm UW}$ is the partition function and $\hat{H}_s$ is the original system Hamiltonian in Eq. (28). It can be also shown that the Gibbs state is the long-time limit of the weak-coupling BMR-QME simulation [23,24]. In this limit, λ dictates the *rate* to approach the steady state but not its value, as we clearly see in Fig. 4 (magenta dashed-dotted line).

(ii) The RC steady state is defined as

$$\rho^{\rm SS}_{\rm RC} = \frac{1}{Z_{\rm RC}} {\rm Tr}_{\rm RC}\left[e^{-\beta(\hat{H}_s + \Omega \hat{a}^\dagger \hat{a} + \lambda \hat{S}(\hat{a}^\dagger + \hat{a}))}\right] \tag{39}$$

and it clearly has a nontrivial λ dependence: While the *extended system*, which encompasses the RC, thermalizes to a conventional Gibbs state, the state of the spin itself, obtained after the RC is traced out, depends on λ. The RC steady state, [Eq. (39)] is achieved numerically as the long-time solution of RC-QME simulations [13] and in Fig. 4 we present both calculations (cyan). We clarify that the RC-QME value (cyan solid line) is obtained by constructing the Redfield tensor and inverting it as in Eq. (24). In contrast, the RC steady-state result (cyan circles) is reached according to Eq. (39) by constructing the extended system Hamiltonian (and yet truncating the RC to include 11 levels, which is a sufficiently high number to represent the harmonic manifold of the RC), exponentiating the result, and tracing out the RC. These two approaches provide identical values.

(iii) The EFF steady state is

$$\rho^{\rm SS}_{\rm EFF} = \frac{1}{Z_{\rm EFF}} e^{-\beta \hat{H}^{\rm eff}_s(\lambda)}, \tag{40}$$

with the effective system Hamiltonian $\hat{H}^{\rm eff}_s(\lambda)$ given by Eq. (31). This state is tractable *analytically* and it can be evaluated to give a closed-form expression (see Appendix C), culminating in Eq. (C9).

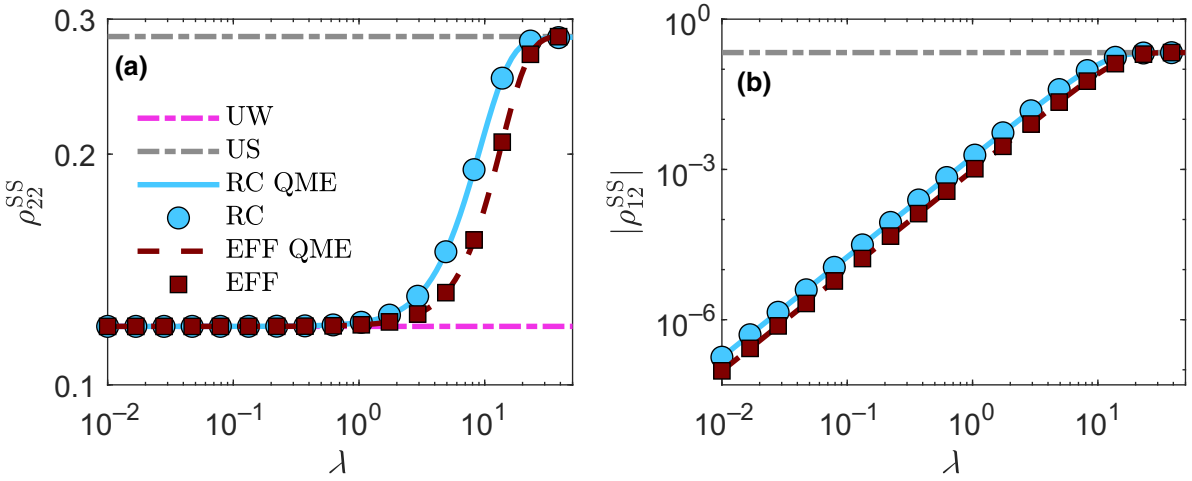

FIG. 4. The thermalization in the generalized spin-boson model. We present (a) the population and (b) the coherence in the eigenbasis of the Hamiltonian of the spin using two limiting cases of the steady state: the ultraweak-coupling limit [Eq. (38)] (UW, magenta dashed-dotted line) and the ultrastrong limit of Ref. [26] (US, light-gray dashed-dotted line). We further show the numerical RC QME, where the Redfield equation is solved after performing a reaction-coordinate mapping (solid line), as well as its steady-state approximation [Eq. (39)] (cyan circles). We also display the EFF-QME results, where the Redfield QME is once again implemented after the RCPT method (dashed line) as well as its steady-state approximation [Eq. (40)] (maroon squares). The parameters are $\Delta = 1$, $\theta = \pi/4$ $\gamma = 0.0071$, $\Omega = 20$, $\Lambda = 1000$, and $T = \Delta/2$.

In Fig. 4, we present both the EFF steady state of Eq. (40) (maroon square) and steady-state simulations based on the EFF-QME method while using the effective Hamiltonian in Eq. (31) (maroon, solid lines). These two calculations agree and we find that the steady-state density matrix depends on λ in a nontrivial manner. Interestingly, the EFF steady state provides excellent qualitative results for *all coupling regimes*: it is exact in the asymptotically weak-coupling regime. It is also exact in the ultrastrong-coupling limit (see Sec. III C). In between, it correctly reproduces the RC steady-state trends, albeit with some deviations in the position of the weak-to-strong crossover. Concretely, the steady state of the conventional spin-boson model ($\theta = \pi/2$) is diagonal, with

$$\rho^{\mathrm{SS}}_{\mathrm{EFF}}(\theta = \pi/2) \propto e^{-\beta \Delta_{\mathrm{eff}}(\lambda)\sigma_z}, \tag{41}$$

where $\Delta_{\mathrm{eff}}(\lambda)$ is given in Eq. (36). The steady state of the intermediate case ($\theta = \pi/4$), presented in Fig. 4, is nondiagonal and thus maintains steady-state coherences:

$$\rho^{\mathrm{SS}}_{\mathrm{EFF}}(\theta = \pi/4) \propto e^{-(1/2)\beta\Delta[(1+e^{-(2\lambda^2/\Omega^2)})\hat{\sigma}_z + (1-e^{-(2\lambda^2/\Omega^2)})\hat{\sigma}_x]}. \tag{42}$$

The proportionality constants in the above expressions are the reciprocals of the partition functions of the respective states, which can be computed by a trace over the system.

(iv) The ultrastrong-limit steady state (US) of Ref. [26] is also plotted in Fig. 4 (light-gray dashed-dotted line). It is given below in Eq. (45). Remarkably, the EFF steady state approaches this limit as $\lambda \to \infty$. We discuss this limit in more detail in Sec. III C.

C. Ultrastrong-coupling limit of the generalized spin-boson model

Focusing now on the ultrastrong-coupling limit with $\lambda \to \infty$, we obtain from the effective-Hamiltonian—RCPT treatment [Eq. (40)] the following steady state:

$$\lim_{\lambda\to\infty} \rho^{\mathrm{SS}}_{\mathrm{EFF}}(\theta) \propto e^{-(\beta\Delta/2)\left[(1+\cos(2\theta))\hat{\sigma}_z + \sin(2\theta)\hat{\sigma}_x\right]}. \tag{43}$$

Thus, at very strong coupling, the conventional model ($\theta = \pi/2$) corresponds to the two levels being equally populated, with zero coherences. In contrast, when the coupling involves noncommuting operators using $\theta = \pi/4$, the RCPT method provides the steady state

$$\lim_{\lambda\to\infty} \rho^{\mathrm{SS}}_{\mathrm{EFF}}(\theta = \pi/4) \propto e^{-(\beta\Delta/2)\left[\hat{\sigma}_z + \hat{\sigma}_x\right]}. \tag{44}$$

Here, the equilibrium state possesses different populations from the standard spin-boson model, as well as nonzero steady-state coherences.

We now recall the ultrastrong steady state derived in Ref. [26] for the same model:

$$\lim_{\lambda\to\infty} \rho^{\mathrm{SS}}_{\mathrm{US}} = \frac{1}{2}\Big[1 - (\hat{\sigma}_x \sin(\theta) + \hat{\sigma}_z \cos(\theta)) \tanh(\beta\Delta\cos(\theta))\Big]. \tag{45}$$

In Appendix C, we prove that the EFF steady state reduces to this expression in the limit as $\lambda \to \infty$.

We further expand on the exact agreement between our RCPT approach and the ultrastrong limit of Ref. [26] by showing, in Fig. 5, the steady-state excited-state populations and the magnitude of the coherences in the limit as $\lambda \to \infty$ as a function of the angle θ. We briefly comment on this agreement, between the EFF steady state and the US steady state [see Eq. (45)]. In Ref. [26], the authors' result was derived by representing the Hamiltonian in the "pointer basis," that is, the eigenbasis of the system operator that is coupled to the bath. Projecting the effective system Hamiltonian in Eq. (14) to the pointer basis, we find that it is exactly equal to the pointer-basis representation of the original system Hamiltonian. Therefore, due to their pointer-basis representations coinciding, we expect the same results for the two methods in the ultrastrong-coupling limit. We derive this fact and provide additional insights in Appendix C.

Figure 5(a) shows an increase in the excited-state population in the ultrastrong-coupling limit with increasing θ. As θ grows, the suppression of the spin splitting becomes more substantial; in the limiting case of $\theta = \pi/2$, the

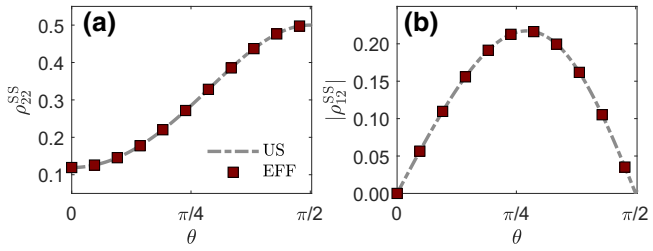

FIG. 5. The ultrastrong-coupling limit of the generalized spin-boson model in the steady state, presenting the (a) population and (b) coherence of the spin as a function of the angle θ, which controls the noncommutativity of operators. We note the exact agreement between the ultrastrong steady state [Eq. (45)] (US, light-gray dashed-dotted line) and our analytical results (maroon squares), calculated using Eq. (43). The parameters are the same as in Fig. 4, with $\lambda \to \infty$.

ground and excited states are equally populated, since they become degenerate in the ultrastrong limit. For lower values of θ, spin-splitting suppression is only one aspect of strong coupling, which explains why we stray from equally populated levels. Furthermore, in Fig. 5(b), we observe that coherences are controlled by the angle θ, with a maximum showing at $\theta = \pi/4$. This can be traced back to the effective system Hamiltonian in Eq. (31), where a new contribution, a coupling-induced tunneling term, is maximized at this angle.

D. Discussion and extensions

The principal far-reaching result of this section is the effective steady state, given in Eq. (40) with its explicit form, given in Eq. (C9). This is a closed-form approximate analytical solution for the steady-state density matrix that captures all coupling regimes, from the asymptotically weak to the ultrastrong limit. The spin-boson example demonstrates that the effective model Hamiltonian, the outcome of the RCPT, provides an accurate description of the equilibrium state of a system coupled to a heat bath, covering the full range of coupling parameters: weak, intermediate, and ultrastrong. The main advantage of the RCPT method is that the equilibrium state is readily obtained by performing the RCPT mapping and there is no need to perform actual open-system dynamics. Another significant result of this section, detailed in Appendix C, is the proof that the MFGS generated by the RCPT approach is *exact* in the ultrastrong-coupling limit and, for *general* systems, beyond the spin model analyzed here in detail.

The EFF steady state can be calculated efficiently for other nontrivial models with steady-state coherences and interactions. The EFF steady state and the resulting partition function allow us to obtain analytical expressions for thermodynamical observables (energy, heat capacity, entropy) in the strong-coupling limit. For example, one could consider a fermionic analog of this study, a quantum dot model with an on-site Coulomb repulsion and strong coupling to the metals. Using the reaction-coordinate method and developing a fermionic analog of the EFF steady state, one may be able to evaluate electrical effects in the highly correlated regime. However, we point out that the development of such a fermionic analog for the EFF steady state is a nontrivial task, due to there not being an equivalent of the polaron transformation for fermions.

IV. HEAT TRANSPORT IN THE NONEQUILIBRIUM SPIN-BOSON MODEL

In this section, we investigate the problem of quantum heat transport in the nonequilibrium spin-boson model. It provides a minimal setting in which to study heat transport at the nanoscale. Such models of thermal transport have recently been experimentally implemented using superconducting quantum circuits [105,106]. The effective model provides an excellent analytical approximation to the quantum heat current, from weak to strong coupling, as has been shown in Ref. [87].

The nonequilibrium spin-boson model is identical to the generalized spin-boson model with $\theta = \pi/2$, except that now the spin couples to two thermal reservoirs ($\alpha = L, R$) held at different temperatures; for a diagramatic representation, see Fig. 1(b). In this model, the two system operators that couple the spin to the different baths commute with each other, allowing for successive polaron transformations to be applied on the two RCs (extracted from each bath), with no conceptual complications.

The Hamiltonian is given by

$$\hat{H} = \Delta\hat{\sigma}_z + \sum_{\alpha=\{L,R\},k} \nu_{\alpha,k}\left(\hat{c}^\dagger_{\alpha,k} + \frac{t_{\alpha,k}}{\nu_{\alpha,k}}\hat{\sigma}_x\right)\left(\hat{c}_{\alpha,k} + \frac{t_{\alpha,k}}{\nu_{\alpha,k}}\hat{\sigma}_x\right). \tag{46}$$

The terms here are analogous to those in Eq. (28), except that now there are two bosonic reservoirs, which are independent and maintained at different thermal states. We follow an identical procedure to Sec. II but now we extract two RCs, one from each bath, and thus we perform two polaron transformations, one for each RC. Since the two baths are coupled via the same system operator, we represent this transformation as a single polaron operator,

$$\hat{U}_P = \hat{U}_{P,L}\hat{U}_{P,R} = e^{[(\lambda_L/\Omega_L)(\hat{a}^\dagger_L - \hat{a}_L) + (\lambda_R/\Omega_R)(\hat{a}^\dagger_R - \hat{a}_R)]\hat{\sigma}_x}. \tag{47}$$

As a consequence of including an additional reservoir, the effective system Hamiltonian is modified from Eq. (33). Namely,

$$\hat{H}^{\rm eff}_s = \Delta e^{-\sum_{\alpha=L,R}(2\lambda^2_\alpha/\Omega^2_\alpha)}\hat{\sigma}_z. \tag{48}$$

The total effective Hamiltonian of the model, Eq. (10) with Eq. (48), is given by

$$\hat{H}^{\rm eff}(\lambda) = \Delta e^{-\sum_{\alpha=L,R}(2\lambda^2_\alpha/\Omega^2_\alpha)}\hat{\sigma}_z + \sum_{\alpha,k}\omega_{\alpha,k}\left(\hat{b}^\dagger_{\alpha,k} - \frac{2\lambda_\alpha f_{\alpha,k}}{\Omega_\alpha\omega_{\alpha,k}}\hat{\sigma}_x\right)\left(\hat{b}_{\alpha,k} - \frac{2\lambda_\alpha f_{\alpha,k}}{\Omega_\alpha\omega_{\alpha,k}}\hat{\sigma}_x\right). \tag{49}$$

Since in the effective model the spin weakly couples to the heat bath, analytical expressions from the weak-coupling limit can be adopted to provide a closed-form expression for the heat current, capturing weak- to strong-coupling behavior [87]. We do not repeat these expressions here

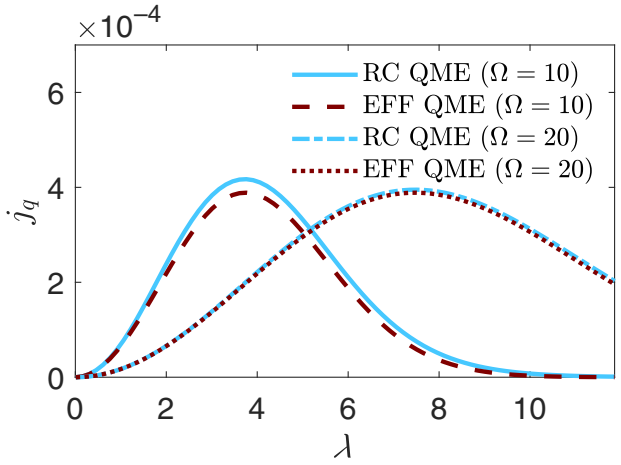

FIG. 6. Quantum heat transport in the nonequilibrium spin-boson model. We present the steady-state heat current computed with the RC-QME method (cyan) and the EFF-QME technique (maroon) at two different RC frequencies, $\Omega = 10$ and $\Omega = 20$. The parameters are $\Delta = 1$, $T_h = \Delta$, $T_c = \Delta/2$, $\gamma = 0.0071$, and $\Lambda = 1000$.

but in Fig. 6 we present calculations of the heat current obtained from the RC-QME method and the EFF-QME technique. Importantly, the two approaches are in excellent agreement. This demonstrates that the effective treatment is appropriate for describing steady-state properties, even in the very-strong-coupling regime. The main nontrivial observation from Fig. 6 is the turnover behavior of the heat current with coupling strength. This phenomenon has been analyzed and demonstrated with powerful numerically exact methods such as in Refs. [54,107–109], as well as with quantum master-equation tools in the polaron frame in, e.g., Refs. [68,69,73,74,98–101,110]. The RCPT method reproduces this nontrival behavior with minimal effort. Fundamentally, we know that transport at weak coupling is sequential and resonant [68,98,99]. Inspecting Eq. (49), we conclude that for large Ω, transport is still sequential and resonant—yet with a spin frequency that is monotonically quenched, revealing the origin of heat-current suppression at strong coupling: When we increase λ, the current first increases due to the enhancement in excitation and relaxation processes transferring energy through the system. However, increasing λ also suppresses the spin splitting and thus the quanta of energy transferred are being quenched. More details on heat transport in this model are given in Ref. [87].

V. AUTONOMOUS QUANTUM ABSORPTION REFRIGERATOR

An autonomous quantum absorption refrigerator (QAR) extracts heat from a cold bath (c) and deposits it in a hot bath (h), assisted by heat input from a so-called work (w) reservoir, obeying $T_c < T_h < T_w$. A canonical model for this machine is made of a quantum "working fluid" with three energy states [111–113], $|n\rangle$, $n = 1, 2, 3$. For a schematic representation, see Fig. 1(c). Transitions between the levels are achieved by absorbing heat or releasing heat to the different thermal reservoirs, with the following system operators: $\hat{S}_c = |1\rangle\langle 2| + \text{h.c.}$, $\hat{S}_w = |2\rangle\langle 3| + \text{h.c.}$, and $\hat{S}_h = |1\rangle\langle 3| + \text{h.c.}$. The total Hamiltonian of this model is

$$\hat{H} = \hat{H}_s + \sum_{\alpha=\{c,w,h\},k} \nu_{\alpha,k} \left(\hat{c}^\dagger_{\alpha,k} + \frac{t_{\alpha,k}}{\nu_{\alpha,k}}\hat{S}_\alpha\right)\left(\hat{c}_{\alpha,k} + \frac{t_{\alpha,k}}{\nu_{\alpha,k}}\hat{S}_\alpha\right). \tag{50}$$

Here, $\hat{c}^\dagger_{\alpha,k}$ ($\hat{c}_{\alpha,k}$) are the bosonic creation (annihilation) operators to generate a quantum of frequency $\nu_{\alpha,k}$ in the αth thermal bath; $t_{\alpha,k}$ are the system-bath coupling energies. The system Hamiltonian is written in the energy basis as

$$\hat{H}_s = \sum_{n=1,2,3} \epsilon_n |n\rangle\langle n|. \tag{51}$$

For the system to act as a refrigerator, that is, extract heat from the cold bath and release it into the hot bath, one needs to tune the energy levels $\epsilon_{1,2,3}$. Without loss of generality, below we use $\epsilon_1 = 0$, $\epsilon_2 = \Delta$ and $\epsilon_3 = 1$ and we adjust Δ to achieve cooling. While the cooling condition and the associated cooling current can be readily obtained assuming weak system-bath coupling [9,10], these calculations become nontrivial once we deviate from this assumption: In Ref. [19], we have used the RC QME, a numerical tool, to locate the cooling window at strong coupling, revealing rich trends.

In what follows, we show that the RCPT approach can be used to provide an analytical expression for the cooling window—assuming for simplicity that only the cold bath is strongly coupled to the three-level quantum system, while the other baths are weakly coupled to it. We thus extract a single reaction coordinate from the cold reservoir and apply the corresponding polaron transformation to the cold RC. This enables analytical expressions for the cooling condition to be obtained from the RCPT method, while not posing new challenges arising from the noncommuting polaron operators.

We comment that we choose to extract the RC from the cold reservoir since it is at a lower temperature than the other baths, hence stronger correlations are expected to survive in this reservoir. The other two contacts are treated in the standard (BMR-QME) weak-coupling fashion. The resulting Hamiltonian upon extracting a reaction coordinate from the cold reservoir is

$$\hat{H}_{\mathrm{RC}} = \hat{H}_s + \sum_{\alpha=\{w,h\},k} \nu_{\alpha,k} \left(\hat{c}^\dagger_{\alpha,k} + \frac{t_{\alpha,k}}{\nu_{\alpha,k}}\hat{S}_\alpha\right)\left(\hat{c}_{\alpha,k} + \frac{t_{\alpha,k}}{\nu_{\alpha,k}}\hat{S}_\alpha\right) + \Omega_c \left(\hat{a}^\dagger_c + \frac{\lambda_c}{\Omega_c}\hat{S}_c\right)\left(\hat{a}_c + \frac{\lambda_c}{\Omega_c}\hat{S}_c\right) + \sum_k \omega_{c,k}\left(\hat{b}^\dagger_{c,k} + \frac{f_{c,k}}{\omega_{c,k}}(\hat{a}^\dagger_c + \hat{a}_c)\right)\left(\hat{b}_{c,k} + \frac{f_{c,k}}{\omega_{c,k}}(\hat{a}^\dagger_c + \hat{a}_c)\right). \tag{52}$$

In this expression, the hot and work reservoirs are unchanged, compared to the initial model given in Eq. (50). The RC transformation acts exclusively on the cold reservoir. It extracts a collective coordinate from that bath of frequency Ω_c, which couples to the system via λ_c. Next, we apply the polaron transformation, $\hat{U}_P = e^{(\lambda_c/\Omega_c)\hat{S}_c(\hat{a}^\dagger_c - \hat{a}_c)}$, to (partially) decouple the cold RC from the three-level system. The resulting Hamiltonian is

$$\hat{H}_{\mathrm{RC-P}} = \hat{U}_P\hat{H}_s\hat{U}^\dagger_P + \sum_{\alpha=\{w,h\},k} \nu_{\alpha,k}\left(\hat{c}^\dagger_{\alpha,k} + \frac{t_{\alpha,k}}{\nu_{\alpha,k}}\hat{U}_P\hat{S}_\alpha\hat{U}^\dagger_P\right)\left(\hat{c}_{\alpha,k} + \frac{t_{\alpha,k}}{\nu_{\alpha,k}}\hat{U}_P\hat{S}_\alpha\hat{U}^\dagger_P\right) + \Omega_c\hat{a}^\dagger_c\hat{a}_c + \sum_k \omega_{c,k}\left(\hat{b}^\dagger_{c,k} + \frac{f_{c,k}}{\omega_{c,k}}\left(\hat{a}^\dagger_c + \hat{a}_c - \frac{2\lambda_c}{\Omega_c}\hat{S}_c\right)\right)\left(\hat{b}_{c,k} + \frac{f_{c,k}}{\omega_{c,k}}\left(\hat{a}^\dagger_c + \hat{a}_c - \frac{2\lambda_c}{\Omega_c}\hat{S}_c\right)\right). \tag{53}$$

Focusing on the subspace with zero excitations in the RC, we arrive at our effective description of the three-level QAR Hamiltonian (ignoring constant shift terms),

$$\hat{H}^{\mathrm{eff}}(\lambda) = \hat{H}_s + \frac{\Delta}{2}\left(e^{-(2\lambda_c^2/\Omega_c^2)} - 1\right)\hat{Q} + \sum_{\alpha=\{w,h\},k} \nu_{\alpha,k}\left(\hat{c}^\dagger_{\alpha,k} + \frac{t_{\alpha,k}}{\nu_{\alpha,k}}e^{-(\lambda_c^2/2\Omega_c^2)}\hat{S}_\alpha\right)\left(\hat{c}_{\alpha,k} + \frac{t_{\alpha,k}}{\nu_{\alpha,k}}e^{-(\lambda_c^2/2\Omega_c^2)}\hat{S}_\alpha\right) + \sum_k \omega_{c,k}\left(\hat{b}^\dagger_{c,k} - \frac{2\lambda_c f_{c,k}}{\Omega_c\omega_{c,k}}\hat{S}_c\right)\left(\hat{b}_{c,k} - \frac{2\lambda_c f_{c,k}}{\Omega_c\omega_{c,k}}\hat{S}_c\right). \tag{54}$$

In this expression, the operator $\hat{Q} = -|1\rangle\langle 1| + |2\rangle\langle 2|$ arises from the action of the polaron transformation on the system Hamiltonian and it represents a shift of the first two energy levels of the QAR.

Inspecting Eq. (54), the overall effect of strong system-bath coupling at the cold contact as observed from the RCPT treatment is nontrivial. (i) The energy difference between the lowest two energy levels (those coupled to the cold bath) is suppressed, $\Delta \to \Delta e^{-(2\lambda_c^2/\Omega_c^2)}$. This effect is similar to the suppression of the spin spacing in the spin-boson model [see Eq. (36)]. (ii) Transitions in the system that are induced by the hot and work baths are suppressed by the cold bath. This effect is highly nontrivial.

The cooling condition specifies regimes in which the system can act as a refrigerator and extract heat from the cold environment. In the weak-coupling limit and using the Born-Markov-Redfield quantum master equation, the cooling condition is [9,10]

$$\frac{\epsilon_2 - \epsilon_1}{\epsilon_3 - \epsilon_1} \le \frac{\beta_h - \beta_w}{\beta_c - \beta_w}. \tag{55}$$

The effect of strong coupling is to *dress* the QAR parameters. In particular, the energy levels of the QAR, ϵ_n, gain a dependence on λ_c. The renormalized energy levels are [see Eq. (54)],

$$\epsilon_1(\lambda_c) = \frac{\Delta}{2}\left(1 - e^{-(2\lambda_c^2/\Omega_c^2)}\right), \tag{56}$$

$$\epsilon_2(\lambda_c) = \frac{\Delta}{2}\left(1 + e^{-(2\lambda_c^2/\Omega_c^2)}\right), \tag{57}$$

$$\epsilon_3(\lambda_c) = 1. \tag{58}$$

The cooling condition in Eq. (55) is derived for the original Hamiltonian in Eq. (50) under the weak-coupling condition. It thus holds for the effective Hamiltonian in Eq. (54) since it has the same form but with renormalized parameters and with weak coupling restored between the effective system and the bath. We thus write down the cooling condition in the strong-coupling regime using the renormalized levels:

$$\frac{\epsilon_2(\lambda) - \epsilon_1(\lambda)}{\epsilon_3(\lambda) - \epsilon_1(\lambda)} = \frac{\Delta e^{-(2\lambda_c^2/\Omega_c^2)}}{1 - (\Delta/2)\left(1 - e^{-(2\lambda_c^2/\Omega_c^2)}\right)} \le \frac{\beta_h - \beta_w}{\beta_c - \beta_w}. \tag{59}$$

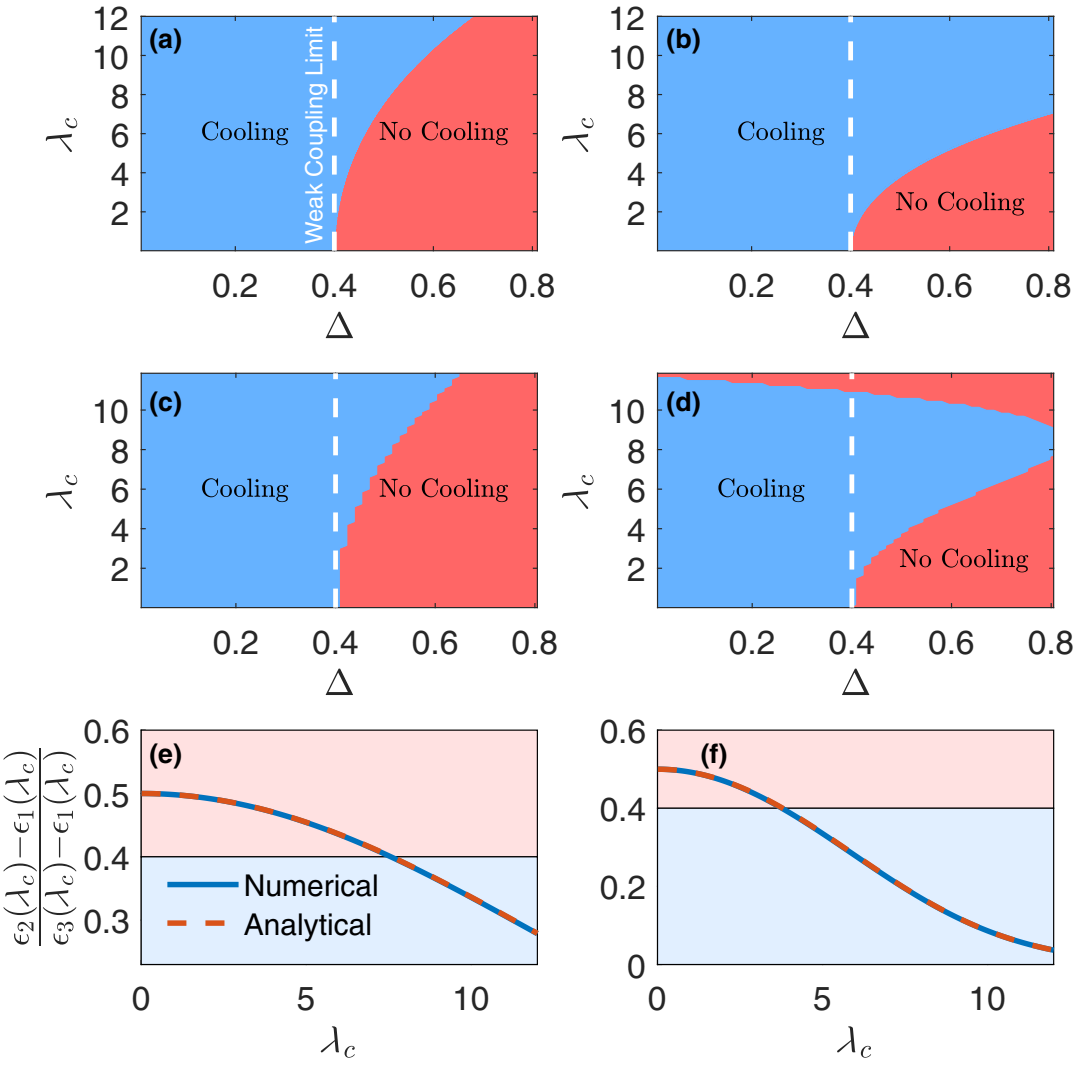

FIG. 7. The cooling window of the three-level autonomous quantum absorption refrigerator. (a),(b) The cooling window calculated *analytically* from the RCPT method using Eq. (59) for (a) $\Omega = 20$ and (b) $\Omega = 10$. (c),(d) The cooling window calculated from the *numerical* RC-QME method for (c) $\Omega = 20$ and (d) $\Omega = 10$. The dashed line marks the boundary of the cooling window in the weak-coupling limit, where cooling takes place for $0 < \Delta < 0.4$. We use reservoir temperatures $T_c = 0.25$, $T_h = 0.5$, and $T_w = 1.5$. (e),(f) A comparison of the eigenvalues calculated from the RCPT method and exact diagonalization of the RC Hamiltonian for (e) $\Omega = 20$ and (f) $\Omega = 10$. Here, $\Delta = 0.5$.

The gap between the lowest two energy levels is suppressed faster with λ_c than the total gap. As a result, at large Δ, where cooling is impossible at weak coupling, we observe cooling once we reach the strong system-reservoir coupling regime. This effect is seen in Fig. 7: The cooling window calculated using Eq. (59) is displayed in Figs. 7(a) and 7(b). It is compared with the cooling window predicted by the weak-coupling limit (to the left of the dashed line at $\Delta = 0.4$). This analytical result is also compared with numerical simulations with the RC-QME method [see Figs. 7(c) and 7(d)].

In these figures, the blue region corresponds to areas where cooling is allowed ($j_c > 0$), whereas the red regions identify the no-cooling regime ($j_c \leq 0$). We find that the effective treatment agrees well with complete simulations for large RC frequency, $\Omega_c = 20$, while for smaller $\Omega_c = 10$, the agreement is not as good, particularly at large λ_c values. This is to be expected, since the RCPT analytical approach relies on Ω_c being the largest energy scale in the problem and deviations are expected once $\lambda_c \approx \Omega_c$.

We comment that deviations between the two approaches are not attributed to problems in capturing the eigenspectrum of the QAR at strong coupling. Figures 7(e) and 7(f) show the left-hand side of the cooling inequality and we compare the analytical expression in Eq. (59) with the effective energies to the numerical value computed by taking the three lowest eigenvalues of the Hamiltonian in Eq. (52). We observe perfect agreement even at large λ_c.

This correspondence reveals that the RCPT method fails to capture the cooling window at small Ω due to transitions missing in the method, the result of the energy truncation involved. For example, leakage effects, with heat flowing directly from the work to the cold bath, are missing in the effective Hamiltonian [19].

Equation (59) demonstrates the remarkable predictive power of the RCPT method. Since strong-coupling effects are now embedded in the energy levels of the system, a wealth of results describing performance bounds on weakly coupled systems can be effortlessly extended to the strong-coupling regime.

VI. PHONON-ASSISTED THERMOELECTRIC ENGINES

In this section, we explore another nontrivial application of the RCPT technique to obtain a deeper understanding of phonon-assisted electron transport and thermoelectric generation in quantum dot setups. In this model, the RC and the subsequent polaron transformation are applied to a bosonic (phonon) reservoir that is strongly coupled to the electronic degrees of freedom (quantum dots) of the system. These quantum dots are assumed to weakly hybridize with voltage-biased and temperature-biased fermionic environments (metals) responsible for both charge and energy currents flowing in the junction. A schematic representation of the model is given in Fig. 1(d).

As we show in this section, using the RCPT method on the phonon-assisted charge transport model, we gain three outcomes. (i) We bypass expensive simulations while treating strong-coupling effects nonperturbatively. (ii) We analytically distill impacts of strong couplings from the renormalization of parameters in the effective Hamiltonian. (iii) We achieve closed-form expressions for transport characteristics, here focusing on the efficiency of a thermoelectric power generator. As for physical observables, the RCPT method provides excellent predictions not only for the averaged charge current but also for its fluctuations, as well as for the energy current.

A. Model and the derivation of the effective Hamiltonian

The literature includes many theoretical proposals for phonon-assisted quantum-dot-based thermoelectric generators (see, e.g., Refs. [91,114–118]). In Refs. [119–121], for instance, phonon-assisted conduction and thermoelectric generation have been analyzed in double-quantum-dot devices. In those studies, however, the hybridization of the dots to the metal electrodes has been assumed to be strong but the electronic states of the quantum dots only perturbatively couple to phonons; computationally extensive simulations in Ref. [53] explore nonperturbative electron-phonon coupling effects.

In the present study and following Ref. [91], we assume that the coupling of the quantum dots to the metal electrodes is weak and can be handled in a perturbative manner by a second-order BMR QME. The coupling of the quantum dot to a phonon bath is, however, strong and this interaction, which is treated with the RCPT method, is essential for facilitating charge transport.

The Hamiltonian of the double quantum dot is written in the $|G\rangle, |L\rangle, |R\rangle, |D\rangle$ basis, which corresponds to the states with neither dots being occupied, the left dot only occupied, the right dot only occupied, and both dots occupied, respectively. In this basis, the total Hamiltonian is represented as

$$\begin{aligned}\hat{H} = {} & \epsilon_L|L\rangle\langle L| + \epsilon_R|R\rangle\langle R| + (\epsilon_L + \epsilon_R + U)|D\rangle\langle D| + \sum_k \epsilon_{k,L}\hat{c}^\dagger_{k,L}\hat{c}_{k,L} + \sum_k \epsilon_{k,R}\hat{c}^\dagger_{k,R}\hat{c}_{k,R} \\ & + \sum_k \left[(|R\rangle\langle D| - |G\rangle\langle L|)h_{k,L}\hat{c}^\dagger_{k,L} + h.c.\right] + \sum_k \left[(|L\rangle\langle D| + |G\rangle\langle R|)h_{k,R}\hat{c}^\dagger_{k,R} + \text{h.c.}\right] \\ & + \sum_q \nu_q \left(\hat{d}^\dagger_q + \frac{t_q}{\nu_q}(|L\rangle\langle R| + h.c.)\right)\left(\hat{d}_q + \frac{t_q}{\nu_q}(|L\rangle\langle R| + \text{h.c.})\right). \end{aligned} \tag{60}$$

For more details on this model, see Ref. [91]. In the above expression, $\epsilon_{L,R}$ are the energies of the left and right quantum dots and U is the Coulomb interaction energy when both quantum dots are occupied. The fermionic reservoirs are coupled to the dots with a coupling strength $h_{k,L/R}$; here, the creation (annihilation) operators $\hat{c}^\dagger_{k,\alpha}$ ($\hat{c}_{k,\alpha}$) create (annihilate) an electron in the fermionic lead $\alpha = L, R$ with energy $\epsilon_{k,\alpha}$. We assume a linear dispersion relation for the electronic energy with a wide band of a constant density of states. The last line in Eq. (60) describes electron tunneling between the two dots—assisted by a phonon bath. The phononic degrees of

freedom are described by creation (annihilation) operators $\hat{d}_q^\dagger$ ($\hat{d}_q$). Here, q identifies a normal mode with frequency ν_q coupled to electronic transitions between the dots with the coupling energy t_q.

Following Ref. [91], we introduce a compact notation for the system operators on the double-quantum-dot Hilbert space, $\hat{A}_1 = -|G\rangle\langle L| + |R\rangle\langle D|$, $\hat{A}_2 = -|L\rangle\langle G| + |D\rangle\langle R|$, $\hat{A}_3 = |G\rangle\langle R| + |L\rangle\langle D|$, $\hat{A}_4 = |R\rangle\langle G| + |D\rangle\langle L|$, $\hat{S} = |L\rangle\langle R| + |R\rangle|L\rangle$, $\hat{L} = |L\rangle\langle L|$, $\hat{R} = |R\rangle\langle R|$, and $\hat{D} = |D\rangle\langle D|$. We allow phonons to strongly couple to electron. We perform a reaction-coordinate transformation on the phononic degrees of freedom to extract a collective phonon coordinate and add it to the system Hamiltonian. The dot-metal hybridization is assumed to be weak (although in principle, one can also perform the RC mapping on the electronic energies).

After the polaron transform and the truncation of the RC mode, we arrive at our effective Hamiltonian, exhibiting strong electron-phonon coupling through renormalized parameters and new coupling terms. After neglecting constant terms, we obtain

$$\begin{aligned}\hat{H}^{\rm eff}(\lambda) = &\left[\epsilon_L \cosh\left(\frac{\lambda^2}{\Omega^2}\right) + \epsilon_R \sinh\left(\frac{\lambda^2}{\Omega^2}\right)\right] e^{-(\lambda^2/\Omega^2)}\hat{L} + \left[\epsilon_R \cosh\left(\frac{\lambda^2}{\Omega^2}\right) + \epsilon_L \sinh\left(\frac{\lambda^2}{\Omega^2}\right)\right] e^{-(\lambda^2/\Omega^2)}\hat{R} \\ &+ (\epsilon_L + \epsilon_R + U)\hat{D} + \sum_q \omega_q \left(\hat{b}_q^\dagger - \frac{2\lambda f_q}{\Omega\omega_q}\hat{S}\right)\left(\hat{b}_q - \frac{2\lambda f_q}{\Omega\omega_q}\hat{S}\right) + \sum_k \left[\hat{A}_1 h_{k,L} e^{-(\lambda^2/2\Omega^2)}\hat{c}_{k,L}^\dagger + \hat{A}_2 h_{k,L}^* e^{-(\lambda^2/2\Omega^2)}\hat{c}_{k,L}\right] \\ &+ \sum_k \left[\hat{A}_3 h_{k,R} e^{-(\lambda^2/2\Omega^2)}\hat{c}_{k,R}^\dagger + \hat{A}_4 h_{k,R}^* e^{-(\lambda^2/2\Omega^2)}\hat{c}_{k,R}\right] + \sum_k \epsilon_{k,L}\hat{c}_{k,L}^\dagger\hat{c}_{k,L} + \sum_k \epsilon_{k,R}\hat{c}_{k,R}^\dagger\hat{c}_{k,R}. \end{aligned} \tag{61}$$

Here, Ω and λ are parameters of the spectral density function of the phonon bath, describing the central frequency of the bath and its coupling energy to the electronic system [see Eq. (15)]. However, after the RCPT procedure, these bath parameters are imprinted into the model Hamiltonian itself. Furthermore, since we assume that the spectral density function is narrow and that $\lambda < \Omega$, the residual phonon bath only weakly couples to the system, as in Eq. (12). Intermediate steps in the calculation are presented in Appendix D.

Inspecting the Hamiltonian in Eq. (61) and comparing it to the original expression in Eq. (60), the effects of the RCPT mapping can be summarized as follows. (i) The energy levels of the electronic dots are renormalized by the coupling to phonons such that they approach equal values at strong coupling. (ii) The coupling of the phonon bath to the dots is dressed (weakened) by the factor λ/Ω. (iii) Electron tunneling from the metals to the dots is exponentially suppressed.

To expound on the impact of strong system-bath couplings, we define the renormalized energy parameters,

$$\epsilon_L(\lambda) = \left[\epsilon_L \cosh\left(\frac{\lambda^2}{\Omega^2}\right) + \epsilon_R \sinh\left(\frac{\lambda^2}{\Omega^2}\right)\right] e^{-(\lambda^2/\Omega^2)}, \tag{62}$$

$$\epsilon_R(\lambda) = \left[\epsilon_R \cosh\left(\frac{\lambda^2}{\Omega^2}\right) + \epsilon_L \sinh\left(\frac{\lambda^2}{\Omega^2}\right)\right] e^{-(\lambda^2/\Omega^2)}, \tag{63}$$

$$h_{k,L}(\lambda) = h_{k,L} e^{-(\lambda^2/2\Omega^2)}; \quad h_{k,R}(\lambda) = h_{k,R} e^{-(\lambda^2/2\Omega^2)}, \tag{64}$$

corresponding to the phonon-dressed quantum dot energies, $\epsilon_{L,R}(\lambda)$ and the phonon-dressed metal-dot hybridizations, $h_{k,L}(\lambda)$ and $h_{k,R}(\lambda)$.

In Fig. 8, we show these renormalized parameters, which are strongly affected by the electron-phonon coupling when λ approaches Ω. For a system configured with $\epsilon_R = 2$ and $\epsilon_L = 0$, we again observe level renormalization as a staple of strong coupling in this model. Here,

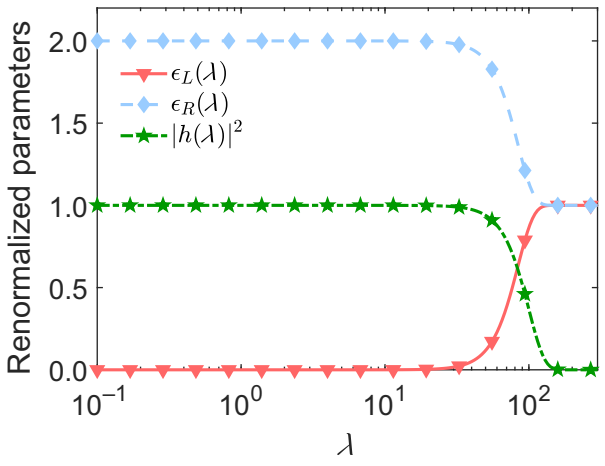

FIG. 8. The effective coupling-dressed parameters in the phonon-assisted quantum dot thermoelectric generator. We display the energy of the left dot (triangle) and the right dot (diamond) and the magnitude squared of the coupling energy between the dots and the fermionic baths (star), as calculated from Eqs. (62)–(64). The parameters (without dressing) are $\epsilon_R = 2$, $\epsilon_L = 0$, $|h|^2 = 1$, and $\Omega = 100$.

the quantum dot energies approach their average values at strong coupling. Furthermore, we also observe a suppression of the dot-metal hybridization as the coupling of electrons to the phonon bath is increased, which is notable, since the RC mapping does not involve the fermionic reservoirs. This is indeed a polaronic effect, with the electrons being slowed down due to polaron formation on the dots. As we show below with benchmarking, the RCPT method performs extremely well in this model. It quantitatively captures the significant features of the model even as λ becomes comparable to Ω, a regime that is not guaranteed to be properly described by the RCPT.

B. Charge current and its noise

We now turn to study charge transport in the model. The quantum dot system is coupled to two metal electrodes and a phonon bath and one could use this setup to investigate numerous aspects of quantum transport, such as the behavior of the charge current and its fluctuations as a function of voltage and electron-phonon couplings, with all baths maintained at the same temperature. The system can be also tuned to act as a thermoelectric power generator when applying a temperature difference counteracting the voltage bias. To study this function, we follow Ref. [91] and investigate the same setup. The left metal is set hot and the right side is cold, $T_L > T_R$. However, the chemical potentials of the electrodes are tuned with the opposite polarity, $\mu_L < \mu_R$. As for the temperature of the phonon bath T_{ph}, we set it here to be equal to T_R but one could imagine other situations as described in Ref. [91]. The metal-molecule hybridization is defined as

$$\Gamma_L(\epsilon) = 2\pi \sum_k |h_{k,L}|^2 \delta(\epsilon - \epsilon_{k,L}) \tag{65}$$

and a similar expression is used to define $\Gamma_R(\epsilon)$. We assume that these parameters are energy independent and we work in the weak metal-dot coupling limit such that $\Gamma_{L,R} \ll T_{L,R}$. As for the phonon bath, it is described by a Brownian spectral function with the peak frequency at Ω, Eq. (15). After the mapping, the residual bath couples weakly to the quantum dots, with an Ohmic spectral function.

In Fig. 9, we display the mean charge current and its fluctuations as a function of the electron-phonon coupling strength, λ. We calculate the charge current using Eq. (26), presenting it here with the brackets, $\langle j_e \rangle$, to emphasize that this is the mean current; using a full-counting statistics approach, we also calculate the current noise, denoted here by $\langle\langle j_e^2 \rangle\rangle = \langle j_e^2 \rangle - \langle j_e \rangle^2$. Technical details on how to calculate currents and noise in the model are given in Ref. [91] and we do not repeat them here.

We present results using three methods: BMR QME, which is valid at weak electron-phonon coupling only; RC QME, a numerical tool simulating transport [based on Eq. (D1)], which is expected to hold even for large λ; and the EFF-QME method using the effective Hamiltonian in Eq. (61), then simulating current with the BMR-QME method. Focusing in Fig. 9 on trends as a function of the electron-phonon coupling strength, we note the excellent agreement between the latter two techniques, showcasing the excellent performance of the RCPT method compared to full simulations.

The RCPT method is not only remarkably computationally efficient (as we do not need to pay any computational cost for working in the strong-coupling limit) but, furthermore, it clarifies the origins of (i) the significant enhancement of the current at intermediate electron-phonon coupling compared to the weak-coupling limit

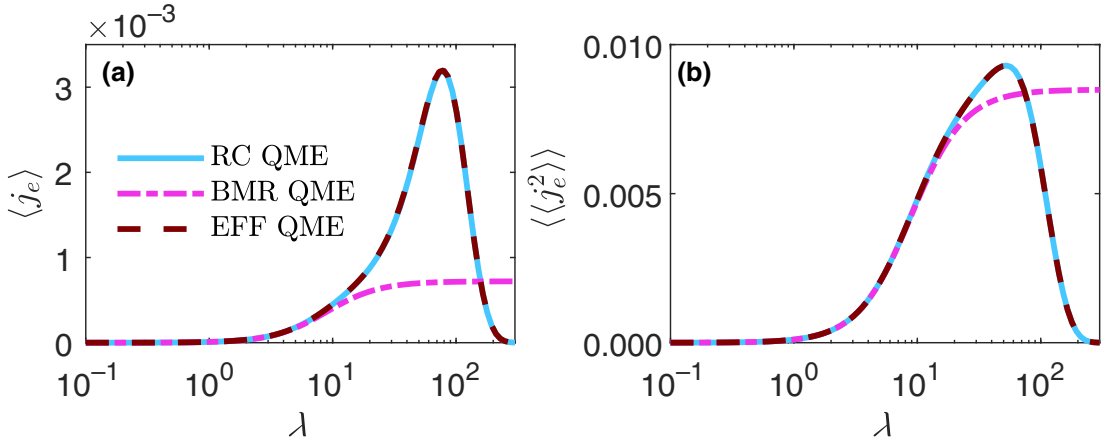

FIG. 9. A phonon-assisted quantum dot thermoelectric power generator. (a) The mean steady-state charge current flowing left to right (positive) and (b) the current fluctuations. The parameters are $\epsilon_R = 2$, $\epsilon_L = 0$, $T_L = 10$, $T_R = 1$, $\Omega = 100$, $\mu_L = -0.3$ $\mu_R = -0.2$, $V = \mu_R - \mu_L = 0.1$, $T_{\rm ph} = 1$, and $2\pi\gamma\Omega = 100$ and the metal-dot hybridization energies are $\Gamma_L = \Gamma_R = 0.1$, all in units of T_R.

and (ii) the complete suppression of charge current at the ultrastrong-coupling limit, as we discuss next.

At weak electron-phonon coupling, the current grows trivially with λ due to the increasing coupling between the dots and the phonon bath (as in the weak-coupling scheme) assisting transport. In the intermediate regime (here, around $\lambda = 50$), the current shoots up, contrasting with the behavior at weak coupling. The reason for this strong enhancement of the current is made clear when looking at the effective Hamiltonian in Eq. (61). As we increase the electron-phonon coupling, the energy levels of the quantum dots approach degeneracy, reaching their mean value $(\epsilon_L + \epsilon_R)/2$ in the ultrastrong-coupling limit. Evening up the energy levels—closing their gap—is beneficial for charge transport. However, at the same time, the metal-quantum dot tunneling elements $|h(\lambda)|^2$ are exponentially suppressed with λ. In the polaron picture, this effect is well known: Unlike the bare electron, an electron dressed by lattice vibrations stabilizes and it requires the "reorganization energy" to hop. The combination of these effects leads to the turnover behavior of the current and its eventual exponential suppression with λ. It is significant to note that besides the mean current, its fluctuations are also excellently captured by the RCPT method, similarly showing a corresponding turnover behavior.

C. Thermoelectric efficiency at strong coupling: Simulations and analytical results

Using the RCPT formalism, we next simulate the charge $\langle j_e \rangle$ and energy currents $\langle j_u \rangle$ arriving from the hot metal, as well as the associated heat current $\langle j_q \rangle = \langle j_u \rangle - \mu_L \langle j_e \rangle$. Combining these currents, we assess the efficiency of the thermoelectric generator, defined as

$$\eta \equiv \frac{P}{\langle j_q \rangle}, \tag{66}$$

with the power extracted $P \equiv \langle j_e \rangle (\mu_R - \mu_L)$. The efficiency is bounded by the Carnot limit, $\eta_C = 1 - (T_c/T_h)$, where $T_{c,h}$ are the temperatures of the cold and hot baths. Nontrivial questions concern how the thermoelectric efficiency depends on voltage and how it is modified by the electron-phonon coupling energy.

In Fig. 10, we look at the dependence of the mean charge current, the mean heat current, and the power output on the applied voltage bias between the right and left leads ($V = \mu_R - \mu_L$). Here, μ_R is varied while μ_L is kept constant. We immediately note the excellent agreement between the RC-QME and EFF-QME methods in Figs. 10(a)–10(c). Using the data for currents, in Fig. 10(d) we plot the thermoelectric efficiency based on Eq. (66). We observe the following: the BMR-QME method predicts that the efficiency will grow linearly with the voltage, reaching the Carnot bound. Indeed, according to a weak-coupling master-equation theory, the efficiency of a thermoelectric generator is given by $\eta = (\mu_R - \mu_L)/(\epsilon_L - \mu_L)$. This reflects the tight-coupling limit between the charge and the heat currents, resulting in their cancellation from the expression for efficiency. Obviously, since the electron-phonon coupling strength is large, the BMR-QME prediction is provided here as a reference point only. Contrasting the characteristic linear trend of weak coupling, the RC-QME simulations show that at finite electron-phonon coupling, the system cannot reach the Carnot efficiency and the efficiency drops drastically to zero as we reach the stopping voltage. Interestingly, the RCPT method with EFF-QME simulations provides accurate results for small-to-intermediate voltage biases but it fails to capture the suppression of efficiency at higher voltage when approaching the stopping voltage. In other words, the EFF-QME method predicts that the efficiency can still reach the Carnot bound but with a different slope—due to the renormalization of parameters. This observation is consistent with the nature of the EFF-QME method. It deploys a weak-coupling theory on an effective Hamiltonian, thus allowing the Carnot bound to be reached. In the ultrastrong-coupling limit and based on Eq. (64) the efficiency is given by $\eta_{\rm US} = (\mu_R - \mu_L)/[(\epsilon_L + \epsilon_R)/2 - \mu_L]$, distinct from the weak-coupling prediction by the value in the denominator.

It is intriguing to note that while both charge and heat currents are seemingly excellently reproduced by the EFF-QME method compared to simulations with the RC QME [see Figs. 10(a)–10(c)], the corresponding thermoelectric efficiencies display marked differences. These deviations can be understood from the inset plots in Figs. 10(b) and 10(c), where we note small deviations in both the heat current and power. According to the inset in Fig. 10(b), the heat current of the RC QME approaches zero at a slightly higher voltage than the EFF QME. Conversely, in the inset in Fig. 10(c), we find that the power output predicted by the RC QME tends toward zero at a slightly lower voltage as compared with the EFF QME. This effect can also be understood as a difference in stopping voltages. The weak-coupling BMR QME predicts a stopping voltage of $V_s = (\epsilon_L - \mu_L)(\beta_R - \beta_L)/\beta_R$ with $\beta_{L,R} = 1/T_{L,R}$ [91]. However, at strong coupling, the stopping voltage increases (in the ultrastrong limit, $\epsilon_L \to (\epsilon_L + \epsilon_R)/2$). This is because the energy level of the left quantum dot increases with λ due to strong-coupling renormalization (see Fig. 8).

D. Discussion

The RCPT method shows excellent predictive power when describing the charge and heat currents and their fluctuations, even at very strong electron-phonon couplings and beyond its rigorous regime of applicability, extending to $\lambda \approx \Omega$. The measure of thermoelectric efficiency, in contrast, is sensitive to small deviations.

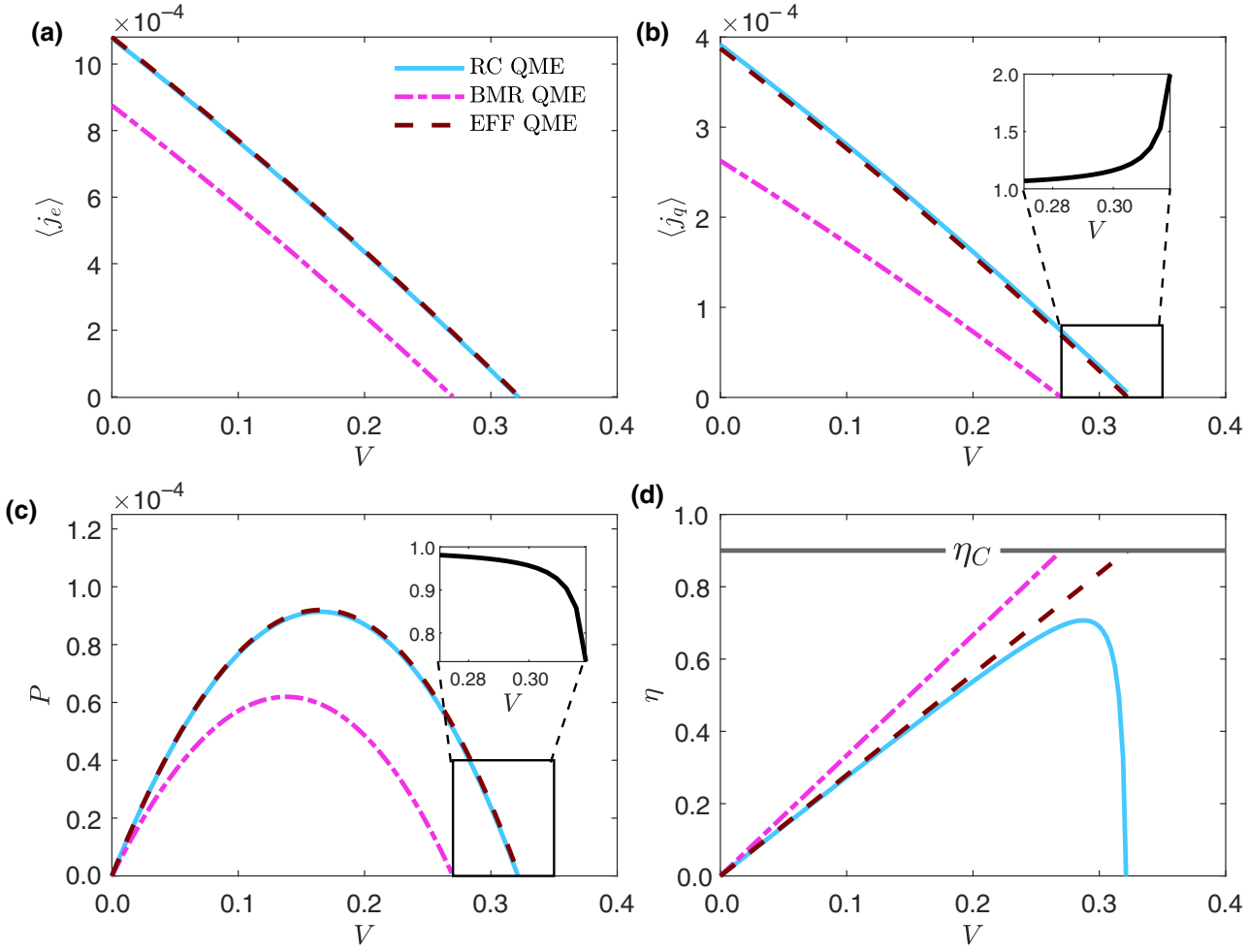

FIG. 10. A phonon-assisted double-quantum-dot thermoelectric power generator. (a) The mean charge current from the left lead (positive) toward the system. (b) The mean heat current from the left reservoir. (c) The power output of the generator, which is given by the charge current times voltage. (d) The thermoelectric efficiency, compared to the Carnot bound η_C. The insets in (b) and (c) present the ratio of currents (RC-QME result over EFF-QME) in the vicinity of the stopping voltage. The parameters are the same as in Fig. 9, with $\lambda = 17.3$ and $\mu_L = -0.3$, while μ_R is varied.

Since the RCPT method still captures only the tight coupling (proportionality) of the currents, its predictions for the efficiency miss the turnover behavior near the stopping voltage. There are many model variants of phonon-assisted charge transport, including the celebrated Anderson-Holstein model. Employing the RCPT framework on canonical models, further including strong hybridization of the dots to the leads, could expose the rich physics of dissipative correlated nonequilibrium fermionic systems.

VII. DISSIPATIVE SPIN CHAINS

Quantum spin models serve a central role in our understanding of quantum many-body systems; specifically, universal aspects of quantum phase transitions in magnetic systems. More recently, *dissipative* spin chains have been studied in, e.g., Refs. [122–128], motivated by applications in quantum information processing and spintronics, as well as real-world experiments simulating spin lattices with cold atoms [129].

We show here that the RCPT method can be readily used to study the properties of dissipative spin chains, namely, their spin polarization and heat transport behavior. We present the theory on a one-dimensional N-site Heisenberg model under a magnetic field. In simulations, we exemplify the theory on a two-qubit system coupled via a general XYZ Ising interaction. Our main result is that due to the impact of strong dissipation, the XX model approaches the Ising model Hamiltonian at strong bath coupling. Thus, dissipation can mask distinct features of spin-chain models.

The Hamiltonian of a dissipative Heisenberg chain with N sites is written as

$$\hat{H} = \sum_{\alpha=1}^{N} \Delta_\alpha \hat{\sigma}_z^\alpha + \sum_{i\in\{x,y,z\}} \sum_{\alpha=1}^{N-1} J_i \hat{\sigma}_i^\alpha \hat{\sigma}_i^{\alpha+1} + \sum_{\alpha=1}^{N} \sum_k \nu_{\alpha,k} \left(\hat{c}_{\alpha,k}^\dagger + \frac{t_{\alpha,k}}{\nu_{\alpha,k}} \hat{\sigma}_x^\alpha\right)\left(\hat{c}_{\alpha,k} + \frac{t_{\alpha,k}}{\nu_{\alpha,k}} \hat{\sigma}_x^\alpha\right). \tag{67}$$

In this expression, Δ_α represents the spin splitting of the αth qubit. The qubits are coupled to each other with strength $J_{x,y,z}$ along the different directions. The qubits are also each coupled to a local bosonic reservoir with modes of frequency $\nu_{\alpha,k}$ at strength $t_{\alpha,k}$. We assume as before that the spectral density functions of these baths are of Brownian form [see Eq. (15)], with Ω_α and λ_α the center of the Brownian functions and the respective qubit-bath coupling strength. Proceeding via the RCPT protocol as outlined in Sec. II, we arrive at the effective Hamiltonian,

$$\begin{aligned}\hat{H}^{\text{eff}}(\lambda_1, \lambda_2, \ldots, \lambda_N) = &\sum_{\alpha=1}^{N} \Delta_\alpha e^{-(2\lambda_\alpha^2/\Omega_\alpha^2)} \hat{\sigma}_z^\alpha \\ &+ \sum_{\alpha=1}^{N-1} \left[J_x \hat{\sigma}_x^\alpha \hat{\sigma}_x^{\alpha+1} + J_y e^{-(2\lambda_\alpha^2/\Omega_\alpha^2)} e^{-(2\lambda_{\alpha+1}^2/\Omega_{\alpha+1}^2)} \hat{\sigma}_y^\alpha \hat{\sigma}_y^{\alpha+1} + J_z e^{-(2\lambda_\alpha^2/\Omega_\alpha^2)} e^{-(2\lambda_{\alpha+1}^2/\Omega_{\alpha+1}^2)} \hat{\sigma}_z^\alpha \hat{\sigma}_z^{\alpha+1}\right] \\ &+ \sum_{\alpha=1}^{N} \sum_k \omega_{\alpha,k} \left(\hat{b}_{\alpha,k}^\dagger - \frac{2\lambda_\alpha f_{\alpha,k}}{\Omega_\alpha \omega_{\alpha,k}} \hat{\sigma}_x^\alpha\right)\left(\hat{b}_{\alpha,k} - \frac{2\lambda_\alpha f_{\alpha,k}}{\Omega_\alpha \omega_{\alpha,k}} \hat{\sigma}_x^\alpha\right).\end{aligned} \tag{68}$$

The effective Hamiltonian depends on all λ_α and Ω_α, although we highlight the dependence on the former. For details on the intermediate steps in the RCPT method, see Appendix E. The residual coupling of the qubits to their baths is now weak, as explained in Sec. II.

Inspecting the Hamiltonian in Eq. (68), we note that the suppression of the spin splitting and the interaction parameters J_y and J_z due to the coupling to the baths results in the dissipative XX model approaching the Ising model in the strong-coupling regime. Hence, we discover that models that behave distinctively when isolated from their surroundings become more and more similar as the system-bath interaction is increased.

In what follows, we study the equilibrium and transport properties of the Hamiltonian in Eq. (68) considering only two spins, denoted by L and R, and for two special cases: (i) a transverse-field Ising-type interaction, where $J_z = J_y = 0$ and $J_x = J$, and (ii) an XX-type interaction with $J_z = 0$ and $J_y = J_x = J$. In particular, two-qubit models can be used as components for thermal energy transport, with each qubit coupled to a heat bath at a different temperature [130,131]. For a schematic representation, see Fig. 1(e).

Considering the first line of the Hamiltonian in Eq. (68) in the strong-coupling limit, all but the term proportional to J_x will be exponentially suppressed. Therefore, we observe the following: (i) In the strong-coupling limit, the eigenstates of the effective system Hamiltonian coincide with the eigenstates of $\hat{\sigma}_x^L$ and $\hat{\sigma}_x^R$. This implies that the XX-type model at strong coupling reduces to a description of the Ising model, with zero qubit splitting. (ii) When the qubits are coupled to heat baths at different temperatures, heat current can flow between the baths through the qubits. However, the heat current will be suppressed at strong system-bath coupling since (in the ultrastrong limit) the effective system Hamiltonian commutes with the total Hamiltonian, implying that energy cannot flow in the system. These predictions are arrived at by simply inspecting terms in the effective Hamiltonian in Eq. (68). In Figures 11 and 12, we test these predictions using the numerical RC-QME method. Focusing first on an equilibrium setting with the two baths set at the same temperature, in Fig. 11 we present the spin magnetization as a function of the spin-spin interaction J and the system-bath coupling strength λ. We find that while at weak coupling the XX and the Ising models behave differently as a function of the exchange interaction J, both models follow similar trends as one increases the couplings to the heat baths. Specifically, at weak coupling, the XX model shows a transition from a polarized state to an unpolarized state at $J \approx 1.5$; the Ising model, in contrast, slowly looses polarization with increasing J. At strong dissipation, in contrast, the two models similarly preserve small polarization irrespective of the coupling strength, which is expected given the bath-induced quenching of the spin splitting.

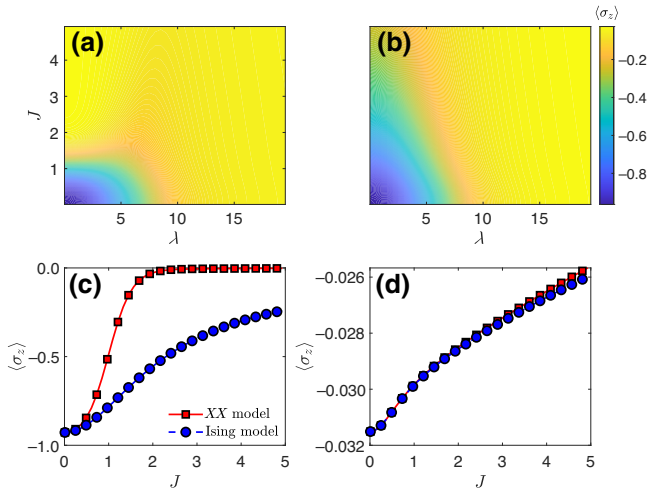

FIG. 11. (a),(b) The equilibrium magnetization in a two-qubit model, plotted as a function of the interaction strength J and the coupling parameter λ using the RC-QME method for both (a) the XX-type and (b) the Ising-type interactions. (c),(d) Cuts of the contour at weak and strong λ, respectively: (c) $\lambda = 1.5$; (d) $\lambda = 17$. The parameters are $\Delta_L = \Delta_R = 1$, $T_L = T_R = 0.5$, and $\Omega = 10$.

In Fig. 12, we turn to a nonequilibrium steady-state situation with $T_L \neq T_R$ and present the current of the XX model [Fig. 12(a)] and the Ising model [Fig. 12(b)]. The important quadrant is in the strong-λ weak-J limit, where the currents predicted by the XX and Ising models coincide. In this regime, since J is weak relative to Ω, our RCPT effective treatment is relevant and our prediction of

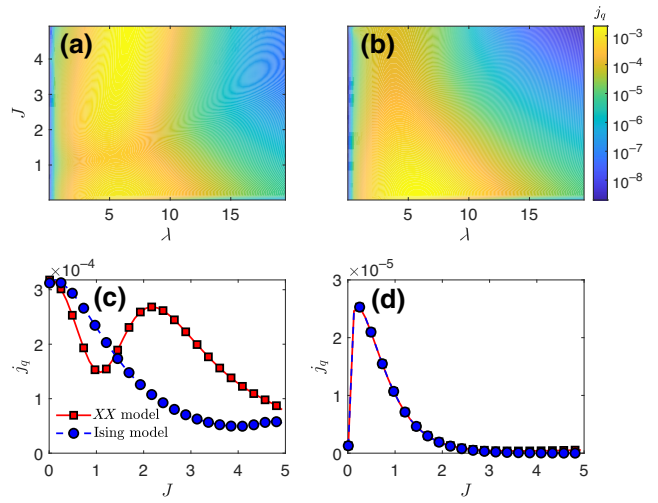

FIG. 12. (a),(b) The steady-state heat current through a two-qubit system, plotted as a function of the interaction strength J and the coupling parameter λ using the RC-QME method for both (a) the XX-type and (b) the Ising-type interactions. (c),(d) Cuts of the contour at weak and strong λ, respectively: (c) $\lambda = 1.5$; (d) $\lambda = 17$. The parameters are $\Delta_L = \Delta_R = 1$, $T_L = 0.5$, $T_R = 1$, and $\Omega = 10$.

the two models coinciding in their behavior and leading to suppressed currents is verified in simulations. Deviations in the currents supported by the two models are apparent in the upper right quadrant, which corresponds to the large-J large-λ limit. Here, since J becomes comparable to Ω, the RCPT framework starts to break down and our predictions of the XX model mapping into the Ising model are not as accurate.

Altogether, the effective-Hamiltonian treatment is a powerful new tool toward studying dissipative spin chains. Besides allowing feasible numerical simulations, the strength of the method lies in it directly building effective Hamiltonians that expose the impact of dissipation on the model parameters and thus on the expected equilibrium phases and transport properties of these paradigmatic systems.

VIII. CONCLUSIONS

We introduce the reaction-coordinate polaron-transformation framework, an analytical-numerical tool for tackling open-quantum-system problems at strong system-bath coupling with harmonic baths. This approach is applicable to a broad range of open quantum systems. While computationally expensive techniques have been developed in recent years to handle strong-coupling effects, including the hierarchical equations of motion (HEOM) formalism, chain-mapping, tensor-network, and path-integral approaches, the RCPT method stands out, with it offering fundamental understanding as to the different impacts of strong couplings, as well as a route for highly economic and reasonably accurate numerical simulations. While the method is introduced and exercised here for systems linearly coupled to the displacements of bosonic-harmonic environments, we are currently devoting efforts toward extending the approach to treat strong-coupling effects between a quantum system and fermionic or spin degrees of freedom. This requires the generalization of the RC transformation and a polaron-like rotation, as well as the introduction of a physically motivated truncation scheme to treat other types of baths.

The essence of our RCPT procedure is that strong system-bath interactions are absorbed and embedded into a (modified) system Hamiltonian, which itself becomes weakly coupled to its surroundings, thus allowing economical simulations and analytical derivations. The procedure involves performing a reaction-coordinate mapping to extract the prominent degrees of freedom from the bath, applying next a polaron transformation to partially decouple the RC from the system, and finally truncating the reaction coordinate. These three steps result in an effective model Hamiltonian with strong system-bath coupling built into the system Hamiltonian.

We employ the RCPT method and study central questions in quantum thermalization, quantum transport, and quantum thermodynamics. Focusing on the steady-state regime, the RCPT method allows us to predict and rationalize trends, derive closed-form expressions quantifying the performance of many-body quantum thermal machines, and perform economic simulations. We exemplify the capacity of the RCPT method with five paradigmatic problems:

(i) We investigate the topic of *quantum thermalization* using the generalized spin-boson model in Sec. III. Our main result via the RCPT procedure is the derivation of a closed-form expression for the thermal equilibrium state of the system. This expression is *exact* in both the weak and the ultrastrong-coupling limits and it further provides qualitatively correct results in the intermediate regime.

(ii) Quantum heat transport is investigated using the spin-boson model in Sec. IV. The RCPT approach provides the characteristic turnover of the heat current with the system-bath coupling energy.

(iii) The impact of strong coupling on the cooling performance of continuous quantum absorption refrigerators is analyzed in Sec. V. Here, the RCPT method allows us to derive analytical expressions for the cooling window, exposing the role of strong coupling.

(iv) The problem of phonon-assisted electron transport is studied in Sec. VI, with a focus on the performance of thermoelectric power generators. The RCPT method provides accurate predictions not only of the charge current but also its fluctuations, revealing a turnover behavior when increasing the coupling to phonons. The method further allows us to write a closed-form expression for the efficiency of the phonon-assisted power generator, valid from linear response to the far-from-equilibrium region (yet, as expected, missing the correct behavior near the stopping voltage).

(v) Dissipative quantum chains are analyzed in Sec. VII. The RCPT method reveals the confluence of different spin-chain models once dissipation is enhanced.

These five canonical models embody many-body interactions, include strong system-bath coupling effects, and encompass rich physics from linear response to the far-from-equilibrium regime. The powerful RCPT method elegantly captures their equilibrium physics and transport characteristics with little effort. While we employ the Redfield QME here to simulate the steady-state behavior of the effective Hamiltonian, other methods can be used in this regard, including numerically exact techniques. In such cases, the effective Hamiltonian offers accelerated convergence due to weakened system-bath coupling, compared to the bare model.

We focus in this study on the steady-state behavior of quantum thermal machines. In future work, we plan to look at how effective models deal with transient and driven dynamics. In this context, complications arise, as the RCPT method may neglect non-Markovian effects due to the truncation of the reaction coordinate. As such, in order to accurately study quantum dynamics, a method that can capture such features is required. Another potential avenue for the RCPT method is the application of iterative mappings, making use of, e.g., numerical spectral density functions for the RC transformation. This would allow studies with spectral density functions that are richer, beyond the Brownian form. More broadly, we envision the development and application of RCPT-inspired mapping methods to understand and simulate light-matter systems, time-dependent driven materials, and interacting fermionic models.

ACKNOWLEDGMENTS

D.S. acknowledges support from a Natural Sciences and Engineering Research Council of Canada (NSERC) Discovery Grant and the Canada Research Chair program. The work of N.A.S. was supported by an Ontario Graduate Scholarship (OGS). We acknowledge fruitful discussions with Janet Anders.

APPENDIX A: CALCULATION OF THE EFFECTIVE SYSTEM HAMILTONIAN

In this appendix, we simplify the expression obtained in Sec. II for the system portion within the total effective Hamiltonian. Our starting point is the subspace of the polaron-dressed system Hamiltonian [see Eq. (13)]:

$$\hat{H}_s^{\rm eff}(\lambda) = \langle 0|e^{(\lambda/\Omega)(\hat{a}^\dagger-\hat{a})\hat{S}}\hat{H}_s e^{-(\lambda/\Omega)(\hat{a}^\dagger-\hat{a})\hat{S}}|0\rangle. \tag{A1}$$

The polaron-transformation operator has a similar mathematical structure to the displacement operator, $D(\alpha) = e^{\alpha\hat{a}^\dagger-\alpha\hat{a}}$, where in our situation, the parameter α is in fact an operator living in the Hilbert space of the system, $\alpha \equiv (\lambda/\Omega)\hat{S}$. We note, that here, α is Hermitian. We use the following properties of the displacement operator: $D(-\alpha) = D^\dagger(\alpha)$ and $D(\alpha)|0\rangle = |\alpha\rangle$, which implies that $D^\dagger(\alpha)|0\rangle = |-\alpha\rangle$ to write the effective system Hamiltonian as

$$\hat{H}_s^{\rm eff}(\lambda) = \langle -\alpha|\hat{H}_s|-\alpha\rangle. \tag{A2}$$

Next, we comment that coherent states can be represented by the eigenstates of the harmonic oscillator $|n\rangle$ as $|\alpha\rangle = e^{-(|\alpha|^2/2)}\sum_{n=0}^{\infty}(\alpha^n/\sqrt{n!})|n\rangle$. In the models examined here, all the elements in α are real and thus we

ignore the absolute-value symbol. Combining these facts, we compute the effective system Hamiltonian,

$$\begin{aligned}\hat{H}_s^{\text{eff}}(\lambda) &= e^{-(\alpha^2/2)}\sum_{n,m}\frac{(-1)^n}{\sqrt{n!}}\langle n|\alpha^n\hat{H}_s\alpha^m|m\rangle\frac{(-1)^m}{\sqrt{m!}}e^{-(\alpha^2/2)}\\ &= e^{-(\alpha^2/2)}\sum_{n}\frac{(-1)^{2n}}{n!}\alpha^n\hat{H}_s\alpha^n e^{-(\alpha^2/2)},\\ &= e^{-(\lambda^2/2\Omega^2)\hat{S}^2}\left(\sum_n\frac{\lambda^{2n}}{\Omega^{2n}n!}\hat{S}^n\hat{H}_s\hat{S}^n\right)e^{-(\lambda^2/2\Omega^2)\hat{S}^2}.\end{aligned} \tag{A3}$$

This is our final expression: in the second line, we make use of the fact that $\hat{H}_s$ and $\hat{S}$ are operators that act on the system Hilbert space only. Therefore, the partial matrix element resolves simply to a Kronecker product in the m and n states.

APPENDIX B: EFFECTIVE-HAMILTONIAN HIGHER-ORDER CONTRIBUTIONS

In this appendix, we explain how to systematically extend the RCPT method and build higher-order contributions to the effective Hamiltonian of the system, given in Eq. (9). This is done by including higher-order excitations to the RC manifold. For example, if we include two levels in the RC, $|0\rangle$ and $|1\rangle$, the effective Hamiltonian becomes a 2×2 matrix,

$$\begin{aligned}\hat{H}_s^{\text{eff},[2]} &= \langle 0|e^{(\lambda/\Omega)(\hat{a}^\dagger-\hat{a})\hat{S}}\hat{H}_s e^{-(\lambda/\Omega)(\hat{a}^\dagger-\hat{a})\hat{S}}|0\rangle|0\rangle\langle 0|\\ &+\langle 1|e^{(\lambda/\Omega)(\hat{a}^\dagger-\hat{a})\hat{S}}\hat{H}_s e^{-(\lambda/\Omega)(\hat{a}^\dagger-\hat{a})\hat{S}}|1\rangle|1\rangle\langle 1|\\ &+\langle 0|e^{(\lambda/\Omega)(\hat{a}^\dagger-\hat{a})\hat{S}}\hat{H}_s e^{-(\lambda/\Omega)(\hat{a}^\dagger-\hat{a})\hat{S}}|1\rangle|0\rangle\langle 1|\\ &+\langle 1|e^{(\lambda/\Omega)(\hat{a}^\dagger-\hat{a})\hat{S}}\hat{H}_s e^{-(\lambda/\Omega)(\hat{a}^\dagger-\hat{a})\hat{S}}|0\rangle|1\rangle\langle 0|.\end{aligned} \tag{B1}$$

In the main text, we limit the occupation number of the RC to zero, assuming that $\Omega \gg T$. Here, we compute as an example the matrix element between the kth and pth levels. Such extensions to higher occupations of the RC should allow for a more complete description of the RCPT technique and provide corrections for better numerical accuracy. Therefore, as an extension of Eq. (9), we consider terms of the form

$$\langle k|\hat{H}_s^{\text{eff}}|p\rangle = \langle k|e^{(\lambda/\Omega)(\hat{a}^\dagger-\hat{a})\hat{S}}\hat{H}_s e^{-(\lambda/\Omega)(\hat{a}^\dagger-\hat{a})\hat{S}}|p\rangle. \tag{B2}$$

Note that $|p\rangle = (1/\sqrt{p!})(\hat{a}^\dagger)^p|0\rangle$. We can again reexpress the effective system Hamiltonian in terms of a ground-state expectation value,

$$\langle k|\hat{H}_s^{\text{eff}}|p\rangle = \frac{1}{\sqrt{k!p!}}\langle 0|\hat{a}^k D(\alpha)\hat{H}_s D^\dagger(\alpha)(\hat{a}^\dagger)^p|0\rangle. \tag{B3}$$

Next, we make use of the property of displacement operators, $|0\rangle = D(\alpha)|-\alpha\rangle$. As such, we rewrite our matrix element in terms of coherent state expectation values,

$$\begin{aligned}&\langle k|\hat{H}_s^{\text{eff}}|p\rangle\\ &\quad= \frac{1}{\sqrt{k!p!}}\langle -\alpha|D^\dagger(\alpha)\hat{a}^k D(\alpha)\hat{H}_s D^\dagger(\alpha)(\hat{a}^\dagger)^p D(\alpha)|-\alpha\rangle.\end{aligned} \tag{B4}$$

Furthermore, the use of yet another property of displacement operators, $D^\dagger(\alpha)\hat{a}^k D(\alpha) = (\hat{a}+\alpha)^k$, allows us to displace the RC operators,

$$\langle k|\hat{H}_s^{\text{eff}}|p\rangle = \frac{1}{\sqrt{k!p!}}\langle -\alpha|(\hat{a}+\alpha)^k\hat{H}_s(\hat{a}^\dagger+\alpha^\dagger)^p|-\alpha\rangle. \tag{B5}$$

We note that the parameter α in our expressions is Hermitian. Furthermore, we can express the coherent state in the basis of the harmonic-oscillator-number eigenstates $|-\alpha\rangle = \sum_{m=0}^{\infty}((-1)^m/\sqrt{m!})\alpha^m e^{-(|\alpha|^2/2)}$. Next, we use the binomial theorem to write $(\hat{a}+\alpha)^k = \sum_{l=0}^{k}\binom{k}{l}\hat{a}^l\alpha^{k-l}$. Combining these two manipulations, we write down the matrix element as

$$\langle k|\hat{H}_s^{\text{eff}}|p\rangle = \frac{1}{\sqrt{k!p!}}\sum_{j=0}^{p}\sum_{l=0}^{k}\sum_{n,m=0}^{\infty}\frac{(-1)^{n+m}}{\sqrt{n!m!}}\binom{k}{l}\binom{k}{j}e^{-(|\alpha|^2/2)}\langle n|\hat{a}^l\alpha^{k-l+n}\hat{H}_s\alpha^{p-j+m}(\hat{a}^\dagger)^j|m\rangle e^{-(|\alpha|^2/2)}. \tag{B6}$$

Note the action of the creation operator $(\hat{a}^\dagger)^j|m\rangle = \sqrt{(m+j)!/m!}|m+j\rangle$. Therefore,

$$\langle k|\hat{H}_s^{\text{eff}}|p\rangle = \frac{1}{\sqrt{k!p!}}\sum_{j=0}^{p}\sum_{l=0}^{k}\sum_{n,m=0}^{\infty}\frac{(-1)^{n+m}\sqrt{(m+j)!(n+l)!}}{n!m!}\binom{k}{l}\binom{p}{j}e^{-(|\alpha|^2/2)}\langle n+l|\alpha^{k-l+n}\hat{H}_s\alpha^{p-j+m}|m+j\rangle e^{-(|\alpha|^2/2)} \tag{B7}$$

$$= \frac{1}{\sqrt{k!p!}} \sum_{j=0}^{p} \sum_{l=0}^{k} \sum_{n,m=0}^{\infty} \frac{(-1)^{n+m}\sqrt{(m+j)!(n+l)!}}{n!m!} \binom{k}{l} \binom{p}{j} e^{-(|\alpha|^2/2)} \alpha^{k-l+n} \hat{H}_s \alpha^{p-j+m} e^{-(|\alpha|^2/2)} \delta_{n+l,m+j}. \tag{B8}$$

The Kronecker-delta function implies that $m = n + l - j$. Reindexing the sum over m, we arrive at our final expression:

$$\langle k|\hat{H}_s^{\text{eff}}|p\rangle = \frac{1}{\sqrt{k!p!}} \sum_{j=0}^{p} \sum_{l=0}^{k} \sum_{n=j-l}^{\infty} \frac{(-1)^{2n+l-j}(n+l)!}{n!(n+l-j)!} \binom{k}{l} \binom{p}{j} e^{-(|\alpha|^2/2)} \alpha^{k-l+n} \hat{H}_s \alpha^{p-2j+l+n} e^{-(|\alpha|^2/2)} \tag{B9}$$

$$= \frac{1}{\sqrt{k!p!}} \sum_{j=0}^{p} \sum_{l=0}^{k} \sum_{n=j-l}^{\infty} \frac{(-1)^{l-j}(n+l)!}{n!(n+l-j)!} \binom{k}{l} \binom{p}{j} \left(\frac{\lambda}{\Omega}\right)^{k+p-2j+2n} e^{-(\lambda^2/2\Omega^2)\hat{S}^2} \hat{S}^{k-l+n} \hat{H}_s \hat{S}^{p-2j+l+n} e^{-(\lambda^2/2\Omega^2)\hat{S}^2}. \tag{B10}$$

This expression can be readily computed to provide the higher-order corrections to the effective system Hamiltonian.

APPENDIX C: THE RCPT METHOD IN THE ULTRASTRONG-COUPLING LIMIT

1. Pointer basis equivalence

In Ref. [26], it has been proved that for any system (Hamiltonian $\hat{H}_s$) coupled to a bosonic reservoir in an ultrastrong manner, the mean-force Gibbs state, defined in Eq. (27), is given by

$$\lim_{\lambda\to\infty} \rho_{\text{MFGS}}^{\text{SS}} = \frac{e^{-\beta \sum_m \hat{P}_m \hat{H}_s \hat{P}_m}}{\text{Tr}\left[e^{-\beta \sum_m \hat{P}_m \hat{H}_s \hat{P}_m}\right]}, \tag{C1}$$

where the $\hat{P}_m = |m\rangle\langle m|$ are projection operators on the nondegenerate eigenstates $|m\rangle$ of $\hat{S}$. These eigenstates are also referred to as the pointer basis of the ultrastrong-coupling limit. Recall that $\hat{S}$ is an operator of the system, which couples it to the bath. The eigenenergies of $\hat{S}$ are identified as $\hat{P}_m \hat{S} = \epsilon_m \hat{P}_m$. Equation (C1) is obtained from a pertubative technique in λ^{-1}.

Considering now our RCPT method, we next compute the effective system Hamiltonian in Eq. (14) for an *arbitrary* system, projected onto the eigenbasis of $\hat{S}$,

$$\sum_m \hat{P}_m \hat{H}_s^{\text{eff}}(\lambda) \hat{P}_m$$

$$= \sum_m \hat{P}_m e^{-(\lambda^2/2\Omega^2)\hat{S}^2} \left(\sum_{n=0}^{\infty} \frac{\lambda^{2n}}{\Omega^{2n} n!} \hat{S}^n \hat{H}_s \hat{S}^n\right) e^{-(\lambda^2/2\Omega^2)\hat{S}^2} \hat{P}_m$$

$$= \sum_m e^{-(\lambda^2/\Omega^2)\epsilon_m^2} \left(\sum_{n=0}^{\infty} \frac{\lambda^{2n}}{\Omega^{2n} n!} \hat{P}_m \hat{S}^n \hat{H}_s \hat{S}^n P_m\right)$$

$$= \sum_m e^{-(\lambda^2/\Omega^2)\epsilon_m^2} \left(\sum_{n=0}^{\infty} \frac{\lambda^{2n}}{\Omega^{2n} n!} \epsilon_m^{2n} \hat{P}_m \hat{H}_s \hat{P}_m\right)$$

$$= \sum_m \hat{P}_m \hat{H}_s \hat{P}_m. \tag{C2}$$

Importantly, the final expression is *independent* of the coupling parameter λ. The above derivation shows that the pointer-basis representation of the effective system Hamiltonian is *identical* to the pointer-basis representation of the original system Hamiltonian.

Building on Ref. [26], we know that for any model Hamiltonian—including, in particular, the effective Hamiltonian—the ultrastrong MFGS should be given in the form of Eq. (C1) with the corresponding Hamiltonian. Given the equality in Eq. (C2), we thus conclude that the RCPT transformation should produce the correct-exact MFGS in the ultrastrong-coupling limit.

Altogether, while the RCPT method apparently deviates from the correct MFGS in the intermediate-coupling regime, given the underlying approximations, it builds the *correct* state in the ultrastrong-coupling limit, matching Ref. [26]. A partial understanding of this remarkable result is that in the ultrastrong-coupling limit, the energies of the system renormalize—and yet saturate to values of the order of Δ, the eigenenergies of the original system. This suggests that the effective-Hamiltonian approach should hold even in the ultrastrong-coupling limit. However, a deep intuitive explanation pertaining to the success of the RCPT method in the ultrastrong regime is still missing, as well as an estimate as to the accuracy of the effective-Hamiltonian MFGS in the intermediate regime.

2. Equilibrium state of the generalized spin-boson: From asymptotically weak to ultrastrong

We provide here further mathematical details on the effective mean-force Gibbs state of the generalized spin-boson model discussed in Sec. III. In the main text, we express this state in the form of Eq. (40), where $\hat{H}_s^{\text{eff}}(\lambda)$ is given in terms of a closed-form expression [see Eq. (31)]. Using this Hamiltonian, we may then write the equilibrium state in a convenient form,

$$e^{-\beta\hat{H}_s^{\text{eff}}(\lambda)} = e^{-(1/2)\beta\Delta(\vec{v}\cdot\vec{\sigma})}, \tag{C3}$$

where here $\vec{\sigma} = (\hat{\sigma}_x, \hat{\sigma}_y, \hat{\sigma}_z)$ and

$$\vec{v} = [(1 - e^{(-2\lambda^2/\Omega^2)})\sin(2\theta), 0, (1 + e^{(-2\lambda^2/\Omega^2)}) + (1 - e^{(-2\lambda^2/\Omega^2)})\cos(2\theta)]. \tag{C4}$$

Using properties of the Pauli operators, we may reexpress the effective Gibbs state as

$$e^{-\beta\hat{H}_s^{\text{eff}}(\lambda)} = \cosh\left(\frac{\beta\Delta}{2}|\vec{v}|\right)\hat{I} - (\hat{v}\cdot\vec{\sigma})\sinh\left(\frac{\beta\Delta}{2}|\vec{v}|\right), \tag{C5}$$

where $\hat{v}$ is the unit vector associated with $\vec{v}$ and its magnitude is given by

$$|\vec{v}| = \sqrt{2(1 + e^{-(4\lambda^2/\Omega^2)}) + 2(1 - e^{-(4\lambda^2/\Omega^2)})\cos(2\theta)}. \tag{C6}$$

Therefore, the partition function of the effective mean-force Gibbs state is

$$Z_{\text{eff}} = \text{Tr}e^{-\beta\hat{H}_s^{\text{eff}}(\lambda)} = 2\cosh\left(\frac{\beta\Delta}{2}|\vec{v}|\right). \tag{C7}$$

As a result, we may write the equilibrium state of the system in a compact form as

$$\rho_{\text{eff}}^{\text{SS}} = \frac{1}{2}\left[\hat{I} - \frac{(\vec{v}\cdot\vec{\sigma})}{|\vec{v}|}\tanh\left(\frac{\beta\Delta}{2}|\vec{v}|\right)\right]. \tag{C8}$$

Writing explicitly the full λ and θ dependence of this model, we obtain our final solution for the effective mean-force Gibbs state of the generalized spin-boson model, which is valid for any coupling strength λ from asymptotically weak to ultrastrong:

$$\rho_{\text{eff}}^{\text{SS}} = \frac{1}{2}\left[1 - \frac{(1 - e^{(-2\lambda^2/\Omega^2)})\sin(2\theta)\hat{\sigma}_x + ((1 + e^{(-2\lambda^2/\Omega^2)}) + (1 - e^{(-2\lambda^2/\Omega^2)})\cos(2\theta))\hat{\sigma}_z}{\sqrt{2(1 + e^{-(4\lambda^2/\Omega^2)}) + 2(1 - e^{-(4\lambda^2/\Omega^2)})\cos(2\theta)}}\right.$$
$$\left.\times\tanh\left(\frac{\beta\Delta}{2}\sqrt{2(1 + e^{-(4\lambda^2/\Omega^2)}) + 2(1 - e^{-(4\lambda^2/\Omega^2)})\cos(2\theta)}\right)\right]. \tag{C9}$$

We highlight two limiting cases of Eq. (C9) where our results in Figs. 4 and 5 are validated; namely, (i) the asymptotically weak-coupling limit ($\lambda \to 0$), where we expect our solution to converge to a standard Gibbs state, and (ii) the ultrastrong-coupling limit ($\lambda \to \infty$), where we expect our solution to agree with Eq. (45). In these cases, we obtain

$$\lim_{\lambda\to 0}\rho_{\text{eff}}^{\text{SS}} = \frac{1}{2}(1 - \hat{\sigma}_z\tanh(\beta\Delta)) \propto e^{-\beta\Delta\hat{\sigma}_z} \tag{C10}$$

and

$$\lim_{\lambda\to\infty}\rho_{\text{eff}}^{\text{SS}} = \frac{1}{2}\left\{1 - \left[\hat{\sigma}_x\sin(\theta) + \hat{\sigma}_z\cos(\theta)\right]\tanh(\beta\Delta\cos(\theta))\right\}. \tag{C11}$$

Our asymptotically weak-coupling limit agrees exactly with the standard Gibbs state. Moreover, our ultrastrong result matches the ultrastrong limit of Ref. [26]. Therefore, we prove analytically that the RCPT method generates effective-Hamiltonian models that are exact in both the asymptotically weak and ultrastrong-coupling regimes for the generalized spin-boson model.

APPENDIX D: INTERMEDIATE STEPS IN THE RCPT MAPPING OF PHONON-ASSISTED ELECTRON TRANSPORT

We start with the Hamiltonian in Eq. (60) and describe its mapping to Eq. (61). First, we build from Eq. (60) the total RC Hamiltonian,

$$\begin{aligned}\hat{H}_{\mathrm{RC}} &= \epsilon_L\hat{L} + \epsilon_R\hat{R} + (\epsilon_L+\epsilon_R+U)\hat{D} + \Omega\left(\hat{a}^\dagger + \frac{\lambda}{\Omega}\hat{S}\right)\left(\hat{a} + \frac{\lambda}{\Omega}\hat{S}\right)\\ &+ \sum_q \omega_q\left(\hat{b}_q^\dagger + \frac{f_q}{\omega_q}(\hat{a}^\dagger+\hat{a})\right)\left(\hat{b}_q + \frac{f_q}{\omega_q}(\hat{a}^\dagger+\hat{a})\right)\\ &+ \sum_k\left[\hat{A}_1 h_{k,L}\hat{c}_{k,L}^\dagger + \hat{A}_2 h_{k,L}^*\hat{c}_{k,L}\right] + \sum_k\left[\hat{A}_3 h_{k,R}\hat{c}_{k,R}^\dagger + \hat{A}_4 h_{k,R}^*\hat{c}_{k,R}\right] + \sum_k \epsilon_{k,L}\hat{c}_{k,L}^\dagger\hat{c}_{k,L} + \sum_k \epsilon_{k,R}\hat{c}_{k,R}^\dagger\hat{c}_{k,R}. \end{aligned} \tag{D1}$$

In this expression, λ is the coupling strength between the dots and the RC and Ω is the frequency of the RC. $\hat{a}^\dagger$ ($\hat{a}$) is the creation (annihilation) operator of the RC. The coupling energies between the RC and residual phononic bath modes of frequency ω_q are captured by f_q, while the creation (annihilation) operators of the residual phonon bath are given by $\hat{b}_q^\dagger$ ($\hat{b}_q$).

Continuing with the RCPT procedure, we now apply a polaron transformation to partially decouple the phononic RC and the electronic dots, $\hat{U}_P = e^{(\lambda/\Omega)\hat{S}(\hat{a}^\dagger-\hat{a})}$. This rotation results in the transformed Hamiltonian $\hat{H}_{\mathrm{RC-P}} = \hat{U}_P\hat{H}_{\mathrm{RC}}\hat{U}_P^\dagger$, given by

$$\begin{aligned}\hat{H}_{\mathrm{RC-P}} &= \epsilon_L\hat{U}_P\hat{L}\hat{U}_P^\dagger + \epsilon_R\hat{U}_P\hat{R}\hat{U}_P^\dagger + (\epsilon_L+\epsilon_R+U)\hat{U}_P\hat{D}\hat{U}_P^\dagger + \Omega\hat{a}^\dagger\hat{a}\\ &+ \sum_q \omega_q\left(\hat{b}_q^\dagger + \frac{f_q}{\omega_q}(\hat{a}^\dagger+\hat{a}-\frac{2\lambda}{\Omega}\hat{S})\right)\left(\hat{b}_q + \frac{f_q}{\omega_q}(\hat{a}^\dagger+\hat{a}-\frac{2\lambda}{\Omega}\hat{S})\right)\\ &+ \sum_k\left[\hat{U}_P\hat{A}_1\hat{U}_P^\dagger h_{k,L}\hat{c}_{k,L}^\dagger + \hat{U}_P\hat{A}_2\hat{U}_P^\dagger h_{k,L}^*\hat{c}_{k,L}\right]\\ &+ \sum_k\left[\hat{U}_P\hat{A}_3\hat{U}_P^\dagger h_{k,R}\hat{c}_{k,R}^\dagger + \hat{U}_P\hat{A}_4\hat{U}_P^\dagger h_{k,R}^*\hat{c}_{k,R}\right] + \sum_k \epsilon_{k,L}\hat{c}_{k,L}^\dagger\hat{c}_{k,L} + \sum_k \epsilon_{k,R}\hat{c}_{k,R}^\dagger\hat{c}_{k,R}. \end{aligned} \tag{D2}$$

Since the polaron transformation affects both the dots (through $\hat{S}$) and the RC (through $\hat{a}$), terms affected by the polaron transformation involve both the RC Hilbert space and the double dot. With regard to the RC, we make use of the fact that $\hat{U}_P\hat{a}\hat{U}_P^\dagger = \hat{a} - (\lambda/\Omega)\hat{S}$. To compute terms that involve the quantum dots, we note that Eq. (14) can be readily applied to any operator on the double-dot Hilbert space. We give an example of the transformation to $\hat{L}$, noting that all other terms are computed in an analogous manner. Once the reaction coordinate is truncated to zero occupation, we obtain

$$\langle 0|\hat{U}_P\hat{L}\hat{U}_P^\dagger|0\rangle = e^{-(\lambda^2/2\Omega^2)\hat{S}^2}\left(\sum_{n=0}^{\infty}\frac{\lambda^{2n}}{\Omega^{2n}n!}\hat{S}^n\hat{L}\hat{S}^n\right)e^{-(\lambda^2/2\Omega^2)\hat{S}^2}. \tag{D3}$$

In this case, $\hat{S}^n\hat{L}\hat{S}^n$ is equal to $\hat{L}$ for n even and to $\hat{R}$ for n odd. Furthermore, $\hat{S}^2$ is diagonal in this case. An intermediate step in this derivation gives

$$\langle 0|\hat{U}_P\hat{L}\hat{U}_P^\dagger|0\rangle = \cosh\left(\frac{\lambda^2}{\Omega^2}\right)e^{-(\lambda^2/2\Omega^2)\hat{S}^2}\hat{L}e^{-(\lambda^2/2\Omega^2)\hat{S}^2} + \sinh\left(\frac{\lambda^2}{\Omega^2}\right)e^{-(\lambda^2/2\Omega^2)\hat{S}^2}\hat{R}e^{-(\lambda^2/2\Omega^2)\hat{S}^2}. \tag{D4}$$

Since $e^{-(\lambda^2/2\Omega^2)\hat{S}^2} = |G\rangle\langle G| + e^{-(\lambda^2/2\Omega^2)}|L\rangle\langle L| + e^{-(\lambda^2/2\Omega^2)}|R\rangle\langle R| + |D\rangle\langle D|$, the left dot gets altered with energy renormalization. Furthermore, we obtain a new coupling between the left and right dots,

$$\langle 0|\hat{U}_p\hat{L}\hat{U}_p^\dagger|0\rangle = \cosh\left(\frac{\lambda^2}{\Omega^2}\right)e^{-(\lambda^2/\Omega^2)}\hat{L} + \sinh\left(\frac{\lambda^2}{\Omega^2}\right)e^{-(\lambda^2/\Omega^2)}\hat{R}. \tag{D5}$$

For completeness, we also show the transformation of $\hat{A}_1$, since it is distinct from the last computation:

$$\langle 0|\hat{U}_P\hat{A}_1\hat{U}_P|0\rangle = e^{-(\lambda^2/2\Omega^2)\hat{S}^2}\left(\sum_{n=0}^{\infty}\frac{\lambda^{2n}}{\Omega^{2n}n!}\hat{S}^n\hat{A}_1\hat{S}^n\right)e^{-(\lambda^2/2\Omega^2)\hat{S}^2}. \tag{D6}$$

Here, $\hat{S}^n\hat{A}_1\hat{S}^n$ is equal to zero unless $n = 0$. Therefore,

$$\langle 0|\hat{U}_P\hat{A}_1\hat{U}_P|0\rangle = e^{-(\lambda^2/2\Omega^2)}\hat{A}_1. \tag{D7}$$

The effective model is defined as

$$\hat{H}^{\text{eff}}(\lambda) = \langle 0|\hat{H}_{\text{RC-P}}|0\rangle \tag{D8}$$

and we arrive at Eq. (61).

APPENDIX E: INTERMEDIATE STEPS IN THE RCPT MAPPING OF DISSIPATIVE SPIN CHAINS

In this appendix, we begin from the model Hamiltonian in Eq. (67) and include the intermediate steps in deriving the effective model Hamiltonian in Eq. (68).

Starting with Eq. (67), we apply the RCPT method and extract a reaction coordinate from each reservoir:

$$\begin{aligned}\hat{H}_{\text{RC}} = &\sum_{\alpha=1}^{N}\Delta_\alpha\hat{\sigma}_z^\alpha + \sum_{i\in\{x,y,z\}}\sum_{\alpha=1}^{N-1}J_i\hat{\sigma}_i^\alpha\hat{\sigma}_i^{\alpha+1} + \sum_{\alpha=1}^{N}\Omega_\alpha\left(\hat{a}_\alpha^\dagger + \frac{\lambda_\alpha}{\Omega_\alpha}\hat{\sigma}_x^\alpha\right)\left(\hat{a}_\alpha^\dagger + \frac{\lambda_\alpha}{\Omega_\alpha}\hat{\sigma}_x^\alpha\right)\\ &+\sum_{\alpha=1}^{N}\sum_{k}\omega_{\alpha,k}\left(\hat{b}_{\alpha,k}^\dagger + \frac{f_{\alpha,k}}{\omega_{\alpha,k}}(\hat{a}_\alpha^\dagger + \hat{a}_\alpha)\right)\left(\hat{b}_{\alpha,k} + \frac{f_{\alpha,k}}{\omega_{\alpha,k}}(\hat{a}_\alpha^\dagger + \hat{a}_\alpha)\right),\end{aligned} \tag{E1}$$

where λ_α and Ω_α denote the coupling strength and frequency of the αth reaction coordinate. Next, we perform a polaron transformation on each RC, since the unitary operators commute. Explicitly, it is given as

$$\hat{U}_P = \Pi_{\alpha=1}^{N}\hat{U}_{P,\alpha} = \Pi_{\alpha=1}^{N}e^{(\lambda_\alpha/\Omega_\alpha)(\hat{a}_\alpha^\dagger - \hat{a}_\alpha)\hat{\sigma}_x^\alpha}. \tag{E2}$$

We pause here to note that the study of multiqubit systems is natural for the RCPT because the qubits operate on different Hilbert spaces and $\hat{S}^2 = 1$. As a result, performing multiple polaron transformations and generating the effective model is relatively simple compared to the other models studied in this work. We apply the polaron transformation and arrive at the following Hamiltonian:

$$\begin{aligned}\hat{H}_{\text{RC-P}} = &\sum_{\alpha=1}^{N}\Delta_\alpha\hat{U}_P\hat{\sigma}_z^\alpha\hat{U}_P^\dagger + \sum_{i\in\{x,y,z\}}\sum_{\alpha=1}^{N-1}J_i\hat{U}_P\hat{\sigma}_i^\alpha\hat{\sigma}_i^{\alpha+1}\hat{U}_P^\dagger + \sum_{\alpha=1}^{N}\Omega_\alpha\hat{a}_\alpha^\dagger\hat{a}_\alpha\\ &+\sum_{\alpha=1}^{N}\sum_{k}\omega_{\alpha,k}\left(\hat{b}_{\alpha,k}^\dagger + \frac{f_{\alpha,k}}{\omega_{\alpha,k}}\left(\hat{a}_\alpha^\dagger + \hat{a}_\alpha - \frac{2\lambda_\alpha}{\Omega_\alpha}\hat{\sigma}_x^\alpha\right)\right)\left(\hat{b}_{\alpha,k} + \frac{f_{\alpha,k}}{\omega_{\alpha,k}}\left(\hat{a}_\alpha^\dagger + \hat{a}_\alpha - \frac{2\lambda_\alpha}{\Omega_\alpha}\hat{\sigma}_x^\alpha\right)\right).\end{aligned} \tag{E3}$$

Next, we introduce a shorthand notation where the ket vector $|\mathbf{0}\rangle = |0_1, 0_2, \ldots, 0_N\rangle$ denotes a zero-excitation state of each RC. Since the polaron transformations act on different Hilbert spaces, we can simply apply each truncation separately. Therefore, we should only evaluate the action of the polaron transformation on each Pauli operator $\hat{\sigma}_{x,y,z}$, which is done by employing Eq. (14). First, we note that $[\hat{U}_P, \hat{\sigma}_x^\alpha] = 0$, so the action of the polaron transformation is trivial on $\hat{\sigma}_x$. The transformations of $\hat{\sigma}_z$ and $\hat{\sigma}_y$ are very similar and produce the same outcome. We demonstrate the action on $\hat{\sigma}_y$, noting that we compute analogous expressions for $\hat{\sigma}_z$ in Sec. III:

$$\begin{aligned}\langle\mathbf{0}|\hat{U}_{P,\alpha}\hat{\sigma}_y^\alpha\hat{U}_{P,\alpha}^\dagger|\mathbf{0}\rangle &= e^{-(\lambda_\alpha^2/\Omega_\alpha^2)}\sum_n \frac{\lambda_\alpha^{2n}}{\Omega_\alpha^{2n}n!}(\hat{\sigma}_x^\alpha)^n\hat{\sigma}_y^\alpha(\hat{\sigma}_x^\alpha)^n \\ &= e^{-(\lambda_\alpha^2/\Omega_\alpha^2)}\sum_{n,\text{even}}\frac{\lambda_\alpha^{2n}}{\Omega_\alpha^{2n}n!}\hat{\sigma}_y^\alpha + \sum_{n,odd}\frac{\lambda_\alpha^{2n}}{\Omega_\alpha^{2n}n!}\hat{\sigma}_x^\alpha\hat{\sigma}_y^\alpha\hat{\sigma}_x^\alpha \\ &= e^{-(\lambda_\alpha^2/\Omega_\alpha^2)}\left[\cosh\left(\frac{\lambda_\alpha^2}{\Omega_L^2}\right) - \sinh\left(\frac{\lambda_\alpha^2}{\Omega_\alpha^2}\right)\right]\hat{\sigma}_y^\alpha \\ &= e^{-(2\lambda_\alpha^2/\Omega_\alpha^2)}\hat{\sigma}_y^\alpha. \end{aligned} \tag{E4}$$

The effect of strong system-bath coupling as seen from the RCPT method in this model is again parameter renormalization in both the spin splittings as well as the internal interactions: $\Delta_\alpha \to \Delta_\alpha e^{-(2\lambda_\alpha^2/\Omega_\alpha^2)}$, $J_x \to J_x$, $J_y \to J_y e^{-(2\lambda_\alpha^2/\Omega_\alpha^2)}e^{-(2\lambda_{\alpha+1}^2/\Omega_{\alpha+1}^2)}$, $J_z \to J_z e^{-(2\lambda_\alpha^2/\Omega_\alpha^2)}e^{-(2\lambda_{\alpha+1}^2/\Omega_{\alpha+1}^2)}$. The effective model is defined as

$$\hat{H}^{\text{eff}}(\lambda_1, \lambda_2, \ldots.\lambda_N) = \langle 0_1, 0_2, \ldots 0_N|\hat{H}_{\text{RC}-\text{P}}|0_1, 0_2, \ldots, 0_N\rangle \tag{E5}$$

and we arrive at Eq. (68).

[1] A. Nitzan, *Chemical Dynamics in Condensed Phases: Relaxation, Transfer and Reactions in Condensed Molecular Systems* (Oxford University Press, Oxford, United Kingdom, 2006).

[2] H. P. Breuer and F. Petruccione, *The Theory of Open Quantum Systems* (Oxford University Press, Oxford, United Kingdom, 2007).

[3] D. A. Lidar, Lecture notes on the theory of open quantum systems, ArXiv:1902.00967.

[4] M. A. Nielsen and I. L. Chuang, *Quantum Computation and Quantum Information* (Cambridge University Press, Cambridge, United Kingdom, 2010).

[5] R. Kosloff, Quantum thermodynamics: A dynamical viewpoint, Entropy **15**, 2100 (2013).

[6] R. Alicki and R. Kosloff, in *Thermodynamics in the Quantum Regime: Fundamental Theories of Physics*, edited by F. Binder, L. A. Correa, C. Gogolin, J. Anders, and G. Adesso, Vol. 195 (Springer, Cham, Switzerland, 2018), p. 1.

[7] S. Vinjanampathy and J. Anders, Quantum thermodynamics, Contemp. Phys. **57**, 545 (2016).

[8] J. Goold, M. Huber, A. Riera, L. del Rio, and P. Skrzypczyk, The role of quantum information in thermodynamics—a topical review, J. Phys. A: Math. Theor. **49**, 143001 (2016).

[9] R. Kosloff and A. Levy, Quantum heat engines and refrigerators: Continuous devices, Annu. Rev. Phys. Chem. **65**, 365 (2014).

[10] L. A. Correa, J. P. Palao, D. Alonso, and G. Adesso, Quantum-enhanced absorption refrigerators, Sci. Rep. **4**, 1 (2014).

[11] P. Strasberg, *Quantum Stochastic Thermodynamics Foundations and Select Applications* (Oxford University Press, Oxford, United Kingdom, 2022).

[12] S. Deffner and S. Campbell, *Quantum Thermodynamics: An Introduction to the Thermodynamics of Quantum Information* (Morgan & Claypool, San Rafael, California, 2019).

[13] J. Iles-Smith, N. Lambert, and A. Nazir, Environmental dynamics correlations, and the emergence of noncanonical equilibrium states in open quantum systems, Phys. Rev. A **90**, 032114 (2014).

[14] A. Rivas, Strong Coupling Thermodynamics of Open Quantum Systems, Phys. Rev. Lett. **124**, 160601 (2020).

[15] J. Liu, K. A. Jung, and D. Segal, Periodically Driven Quantum Thermal Machines from Warming up to Limit Cycle, Phys. Rev. Lett. **127**, 200602 (2021).

[16] J. Liu and K. A. Jung, Optimal linear cyclic quantum heat engines cannot benefit from strong coupling, Phys. Rev. E **106**, L022105 (2022).

[17] H. M. Friedman, B. K. Agarwalla, and D. Segal, Quantum energy exchange and refrigeration: A full-counting statistics approach, New J. Phys. **20**, 083026 (2018).

[18] S. Seah, S. Nimmrichter, and V. Scarani, Refrigeration beyond weak internal coupling, Phys. Rev. E **98**, 012131 (2018).

[19] F. Ivander, N. Anto-Sztrikacs, and D. Segal, Strong system-bath coupling reshapes characteristics of quantum thermal machines, Phys. Rev. E **105**, 034112 (2022).

[20] D. Newman, F. Mintert, and A. Nazir, Performance of a quantum heat engine at strong reservoir coupling, Phys. Rev. E **95**, 032139 (2017).

[21] A. Mu, B. K. Agarwalla, G. Schaller, and D. Segal, Qubit absorption refrigerator at strong coupling, New J. Phys. **19**, 123034 (2017).

[22] P. Talkner and P. Hänggi, Colloquium: Statistical mechanics and thermodynamics at strong coupling: Quantum and classical, Rev. Mod. Phys. **92**, 041002 (2020).

[23] G. Guarnieri, M. Kolář, and R. Filip, Steady-State Coherences by Composite System-Bath Interactions, Phys. Rev. Lett. **121**, 070401 (2018).

[24] A. Purkayastha, G. Guarnieri, M. T. Mitchison, R. Filip, and J. Goold, Tunable phonon-induced steady state coherence in a double-quantum-dot charge qubit, npj Quantum Inf. **6**, 27 (2020).

[25] A. Gelzinis and L. Valkunas, Analytical derivation of equilibrium state for open quantum system, J. Chem. Phys. **152**, 051103 (2020).

[26] J. D. Cresser and J. Anders, Weak and Ultrastrong Coupling Limits of the Quantum Mean Force Gibbs State, Phys. Rev. Lett. **127**, 250601 (2021).

[27] W. M. Huang and W. M. Zhang, Nonperturbative renormalization of quantum thermodynamics from weak to strong couplings, Phys. Rev. Res. **4**, 023141 (2022).

[28] G. M. Timofeev and A. S. Trushechkin, Hamiltonian of mean force in the weak-coupling and high-temperature approximations and refined quantum master equations, Int. J. Mod. Phys. A **37**, 2243021 (2022).

[29] A. Trushechkin, Quantum master equations and steady states for the ultrastrong-coupling limit and the strong-decoherence limit, Phys. Rev. A **106**, 042209 (2022).

[30] A. S. Trusheckin, M. Merkli, J. D. Cresser, and J. Anders, Open quantum system dynamics and the mean force Gibbs state, AVS Quantum Sci. **4**, 012301 (2022).

[31] K. Goyal and R. Kawai, Steady state thermodynamics of two qubits strongly coupled to bosonic environments, Phys. Rev. Res. **1**, 033018 (2019).

[32] P. L. Orman and R. Kawai, A qubit strongly interacting with a bosonic environment: Geometry of thermal states, ArXiv:2010.09201.

[33] Y. F. Chiu, A. Strathearn, and J. Keeling, Numerical evaluation and robustness of the quantum mean-force Gibbs state, Phys. Rev. A **106**, 012204 (2022).

[34] T. Chen and Y. C. Cheng, Numerical computation of the equilibrium-reduced density matrix for strongly coupled open quantum systems, J. Chem. Phys. **157**, 064106 (2022).

[35] C. L. Latune, Steady state in ultrastrong coupling regime: Expansion and first orders, Quanta **11**, 53 (2022).

[36] H. Maguire, J. Iles-Smith, and A. Nazir, Environmental Nonadditivity and Franck-Condon Physics in Nonequilibrium Quantum Systems, Phys. Rev. Lett. **123**, 093601 (2019).

[37] D. Gribben, D. M. Rouse, J. Iles-Smith, A. Strathearn, H. Maguire, P. Kirton, A. Nazir, E. M. Gauger, and B. W. Lovett, Exact Dynamics of Nonadditive Environments in Non-Markovian Open Quantum Systems, PRX Quantum **3**, 010321 (2022).

[38] G. G. Giusteri, F. Recrosi, G. Schaller, and G. L. Celardo, Interplay of different environments in open quantum systems: Breakdown of the additive approximation, Phys. Rev. E **96**, 012113 (2017).

[39] H.-D. Meyer, U. Manthe, and L. S. Cederbaum, The multi-configurational time-dependent Hartree approach, Chem. Phys. Lett. **165**, 73 (1990).

[40] H. Wang and M. Thoss, Multilayer formulation of the multiconfiguration time-dependent Hartree theory, J. Chem. Phys. **119**, 1289 (2003).

[41] H. Wang, Multilayer multiconfiguration time-dependent Hartree theory, J. Phys. Chem. A **119**, 7951 (2015).

[42] R. Bulla, T. A. Costi, and T. Pruschke, Numerical renormalization group method for quantum impurity systems, Rev. Mod. Phys. **80**, 395 (2008).

[43] U. Schollwock, The density-matrix renormalization group in the age of matrix product states, Ann. Phys. **326**, 96 (2011).

[44] F. B. Anders and A. Schiller, Real-Time Dynamics in Quantum-Impurity Systems: A Time-Dependent Numerical Renormalization-Group Approach, Phys. Rev. Lett. **95**, 196801 (2005).

[45] A. Kato and Y. Tanimura, in *Thermodynamics in the Quantum Regime—Recent Progress and Outlook*, edited by F. Binder, L. A. Correa, C. Gogolin, J. Anders, and G. Adesso (Springer, Cham, Switzerland, 2018), p. 579.

[46] Y. Tanimura, Numerically "exact" approach to open quantum dynamics: The hierarchical equations of motion (HEOM), J. Chem. Phys. **153**, 020901 (2020).

[47] A. J. Leggett, S. Chakravarty, A. T. Dorsey, M. P. A. Fisher, A. Garg, and W. Zwerger, Dynamics of the dissipative two-state system, Rev. Mod. Phys. **59**, 1 (1987).

[48] N. Makri and D. E. Makarov, Tensor propagator for iterative quantum time evolution of reduced density matrices. I. Theory, J. Chem. Phys. **102**, 4600 (1995).

[49] N. Makri and D. E. Makarov, Tensor propagator for iterative quantum time evolution of reduced density matrices. II. Numerical methodology, J. Chem. Phys. **102**, 4611 (1995).

[50] N. Makri, Small matrix disentanglement of the path integral: overcoming the exponential tensor scaling with memory length, J. Chem. Phys. **152**, 041104 (2020).

[51] N. Makri, Small matrix path integral for system-bath dynamics, J. Chem. Theory Comput. **16**, 4038 (2020).

[52] S. Weiss, J. Eckel, M. Thorwart, and R. Egger, Iterative real-time path integral approach to nonequilibrium quantum transport, Phys. Rev. B **77**, 195316 (2008).

[53] L. Simine and D. Segal, Path-integral simulations with fermionic and bosonic reservoirs: Transport and dissipation in molecular electronic junctions, J. Chem. Phys. **138**, 214111 (2013).

[54] M. Kilgour, B. K. Agarwalla, and D. Segal, Path-integral methodology and simulations of quantum thermal transport: Full counting statistics approach, J. Chem. Phys. **150**, 084111 (2019).

[55] A. Strathearn, P. Kirton, D. Kilda, J. Keeling, and B. W. Lovett, Efficient non-Markovian quantum dynamics using time-evolving matrix product operators, Nat. Commun. **9**, 1 (2018).

[56] E. Gull, A. J. Millis, A. I. Lichtenstein, A. N. Rubtsov, M. Troyer, and P. Werner, Continuous-time Monte Carlo methods for quantum impurity models, Rev. Mod. Phys. **83**, 349 (2011).

[57] G. Cohen, E. Gull, D. R. Reichman, and A. J. Millis, Taming the Dynamical Sign Problem in Real-Time Evolution of Quantum Many-Body Problems, Phys. Rev. Lett. **115**, 266802 (2015).

[58] H. Aoki, N. Tsuji, M. Eckstein, M. Kollar, T. Oka, and P. Werner, Nonequilibrium dynamical mean-field theory and its applications, Rev. Mod. Phys. **86**, 779 (2014).

[59] J. Prior, A. W. Chin, S. F. Huelga, and M. B. Plenio, Efficient Simulation of Strong System-Environment Interactions, Phys. Rev. Lett. **105**, 050404 (2010).

[60] A. F. Chin, A. Rivas, S. F. Huelga, and M. B. Plenio, Exact mapping between system-reservoir quantum models and semi-infinite discrete chains using orthogonal polynomials, J. Math. Phys. **51**, 092109 (2010).

[61] D. Tamascelli, A. Smirne, J. Lim, S. F. Huelga, and M. B. Plenio, Efficient Simulation of Finite-Temperature Open Quantum Systems, Phys. Rev. Lett. **123**, 090402 (2019).

[62] T. Chen, V. Balachandran, C. Guo, and D. Poletti, Steady-state quantum transport through an anharmonic oscillator strongly coupled to two heat reservoirs, Phys. Rev. E **102**, 012155 (2020).

[63] M. Brenes, J. J. Mendoza-Arenas, A. Purkayastha, M. T. Mitchison, S. R. Clark, and J. Goold, Tensor-Network Method to Simulate Strongly Interacting Quantum Thermal Machines, Phys. Rev. X **10**, 031040 (2020).

[64] M. A. Ochoa, A. Bruch, and A. Nitzan, Energy distribution and local fluctuations in strongly coupled open quantum systems: The extended resonant level model, Phys. Rev. B **94**, 035420 (2016).

[65] W. Dou, M. A. Ochoa, A. Nitzan, and J. E. Subotnik, Universal approach to quantum thermodynamics in the strong coupling regime, Phys. Rev. B **98**, 134306 (2018).

[66] W. Dou, J. Bätge, A. Levy, and M. Thoss, Universal approach to quantum thermodynamics of strongly coupled systems under nonequilibrium conditions and external driving, Phys. Rev. B **101**, 184304 (2020).

[67] U. Weiss, *Quantum Dissipative Systems* (World Scientific, Singapore, 1993).

[68] L. Nicolin and D. Segal, Non-equilibrium spin-boson model: Counting statistics and the heat exchange fluctuation theorem, J. Chem. Phys. **135**, 164106 (2011).

[69] D. Segal, Heat transfer in the spin-boson model: A comparative study in the incoherent tunneling regime, Phys. Rev. E **90**, 012148 (2014).

[70] R. J. Silbey and R. A. Harris, Variational calculation of the dynamics of a two level system interacting with a bath, J. Chem. Phys. **80**, 2615 (1984).

[71] S. Jang, Y.-C. Cheng, D. R. Reichman, and J. D. Eaves, Theory of coherent resonance energy transfer, J. Chem. Phys. **129**, 101104 (2008).

[72] C. K. Lee, J. Moix, and J. Cao, Accuracy of second order perturbation theory in the polaron and variational polaron frames, J. Chem. Phys. **136**, 204120 (2012).

[73] C. Wang, J. Ren, and J. Cao, Nonequilibrium energy transfer at nanoscale: A unified theory from weak to strong coupling, Sci. Rep. **5**, 11787 (2015).

[74] C. Wang, J. Ren, and J. Cao, Unifying quantum heat transfer in a nonequilibrium spin-boson model with full counting statistics, Phys. Rev. A **95**, 023610 (2017).

[75] M. Bonitz and A. Filinov, Progress in nonequilibrium Green's functions III, J. Phys.: Conf. Ser. **35**, E01 (2006).

[76] Y. Meir and N. S. Wingreen, Landauer Formula for the Current through an Interacting Electron Region, Phys. Rev. Lett. **68**, 2512 (1992).

[77] N. Bergmann and M. Galperin, Green's functions perspective on nonequilibrium thermodynamics of open quantum systems strongly coupled to baths, Eur. Phys. J. Spec. Top. **230**, 859 (2021).

[78] K. A. Velizhanin, M. Thoss, and H. Wang, Meir-Wingreen formula for heat transport in a spin-boson nanojunction model, J. Chem. Phys. **133**, 084503 (2010).

[79] Y. Yang and C. Q. Wu, Quantum heat transport in a spin-boson nanojunction: Coherent and incoherent mechanisms, Euro. Phys. Lett. **107**, 30003 (2014).

[80] B. K. Agarwalla and D. Segal, Energy current and its statistics in the nonequilibrium spin-boson model: Majorana fermion representation, New J. Phys. **19**, 043030 (2017).

[81] J. Liu, H. Xu, B. Li, and C. Wu, Energy transfer in the nonequilibrium spin-boson model: From weak to strong coupling, Phys. Rev. E **96**, 012135 (2017).

[82] A. Nazir and G. Schaller, in *Thermodynamics in the Quantum Regime: Fundamental Aspects and New Directions*, edited by F. Binder, L. A. Correa, C. Gogolin, J. Anders, and G. Adesso (Springer, Cham, Switzerland, 2019), p. 551.

[83] P. Strasberg, G. Schaller, N. Lambert, and T. Brandes, Nonequilibrium thermodynamics in the strong coupling and non-Markovian regime based on a reaction coordinate mapping, New J. Phys. **18**, 073007 (2016).

[84] K. H. Hughes, C. D. Christ, and I. Burghardt, Effective-mode representation of non-Markovian dynamics: A hierarchical approximation of the spectral density. I. Application to single surface dynamics, J. Chem. Phys. **131**, 024109 (2009).

[85] K. H. Hughes, C. D. Christ, and I. Burghardt, Effective-mode representation of non-Markovian dynamics: A hierarchical approximation of the spectral density II. Application to environment-induced nonadiabatic dynamics, J. Chem. Phys. **131**, 124108 (2009).

[86] J. Iles-Smith, A. G. Dijkstra, N. Lambert, and A. Nazir, Energy transfer in structured and unstructured environments: Master equations beyond the Born-Markov approximations, J. Chem. Phys. **144**, 044110 (2016).

[87] N. Anto-Sztrikacs and D. Segal, Strong coupling effects in quantum thermal transport with the reaction coordinate method, New J. Phys. **23**, 063036 (2021).

[88] N. Anto-Sztrikacs, F. Ivander, and D. Segal, Quantum thermal transport beyond second order with the reaction coordinate mapping, J. Chem. Phys. **156**, 214107 (2022).

[89] L. A. Correa, B. Xu, B. Morris, and G. Adesso, Pushing the limits of the reaction-coordinate mapping, J. Chem. Phys. **151**, 094107 (2019).
[90] D. Newman, F. Mintert, and A. Nazir, Quantum limit to nonequilibrium heat-engine performance imposed by strong system-reservoir coupling, Phys. Rev. E **101**, 052129 (2020).
[91] C. McConnell and A. Nazir, Strong coupling in thermoelectric nanojunctions: A reaction coordinate framework, New J. Phys. **24**, 025002 (2022).
[92] P. Strasberg, G. Schaller, T. L. Schmidt, and M. Esposito, Fermionic reaction coordinates and their application to an autonomous Maxwell demon in the strong-coupling regime, Phys. Rev. B **97**, 205405 (2018).
[93] S. Restrepo, S. Böhling, J. Cerrillo, and G. Schaller, Electron pumping in the strong coupling and non-Markovian regime: A reaction coordinate mapping approach, Phys. Rev. B **100**, 035109 (2019).
[94] C. McConnell and A. Nazir, Electron counting statistics for non-additive environments, J. Chem. Phys. **151**, 054104 (2019).
[95] C. L. Latune, Steady state in strong system-bath coupling regime: Reaction coordinate versus perturbative expansion, Phys. Rev. E **105**, 024126 (2022).
[96] N. Anto-Sztrikacs and D. Segal, Capturing non-Markovian dynamics with the reaction coordinate method, Phys. Rev. A **104**, 052617 (2021).
[97] G. D. Mahan, *Many-Particle Physics* (Kluwer Academic, New York, 2000), 3rd ed..
[98] D. Segal and A. Nitzan, Spin-Boson Thermal Rectifier, Phys. Rev. Lett. **94**, 034301 (2005).
[99] D. Segal, Heat flow in nonlinear molecular junctions: Master equation analysis, Phys. Rev. B **73**, 205415 (2006).
[100] C. Hsieh, J. Liu, C. Duan, and J. Cao, A nonequilibrium variational polaron theory to study quantum heat transport, J. Phys. Chem. C **123**, 17196 (2019).
[101] D. Xu and J. Cao, Non-canonical distribution and non-equilibrium transport beyond weak system-bath coupling regime: A polaron transformation approach, Front. Phys. **11**, 110308 (2016).
[102] D. Segal and A. Nitzan, Conduction in molecular junctions: Inelastic effects, Chem. Phys. **281**, 235 (2002).
[103] F. A. Pollock, D. P. S. McCutcheon, B. W. Lovett, E. M. Gauger, and A. Nazir, A multi-site variational master equation approach to dissipative energy transfer, New J. Phys. **15**, 075018 (2013).
[104] H. Liu, C. Wang, L.-Q. Wang, and J. Ren, Strong system-bath coupling induces negative differential thermal conductance and heat amplification in nonequilibrium two-qubit systems, Phys. Rev. E **99**, 032114 (2019).
[105] A. Ronzani, B. Karimi, J. Senior, Y. C. Chang, J. T. Peltonen, C. D. Chen, and J. P. Pekola, Tunable photonic heat transport in a quantum heat valve, Nat. Phys. **14**, 991 (2018).
[106] J. Senior, A. Gubaydullin, B. Karimi, J. T. Peltonen, J. Ankerhold, and J. P. Pekola, Heat rectification via a superconducting artificial atom, Commun. Phys. **3**, 40 (2020).
[107] K. A. Velizhanin, H. Wang, and M. Thoss, Heat transport through model molecular junctions: A multilayer multiconfiguration time-dependent Hartree approach, Chem. Phys. Lett. **460**, 325 (2008).
[108] K. Saito and T. Kato, Kondo Signature in Heat Transfer via a Local Two-State System, Phys. Rev. Lett. **111**, 214301 (2013).
[109] A. Kato and Y. Tanimura, Quantum heat current under non-perturbative and non-Markovian conditions: Applications to heat machines, J. Chem. Phys. **145**, 224105 (2016).
[110] W. Wu and W.-L. Zhu, Heat transfer in a nonequilibrium spin-boson model: A perturbative approach, Ann. Phys. (NY) **418**, 168203 (2020).
[111] M. T. Mitchison, Quantum thermal absorption machines: Refrigerators engines and clocks, Contemp. Phys. **60**, 164 (2019).
[112] H. Friedman and D. Segal, Cooling condition for multilevel quantum absorption refrigerators, Phys. Rev. E **100**, 062112 (2019).
[113] J. Liu and D. Segal, Coherences and the thermodynamic uncertainty relation: Insights from quantum absorption refrigerators, Phys. Rev. E **103**, 032138 (2021).
[114] J. H. Jiang, M. Kulkarni, D. Segal, and Y. Imry, Phonon thermoelectric transistors and rectifiers, Phys. Rev. B **92**, 045309 (2015).
[115] J. Liu and D. Segal, Thermodynamic uncertainty relation in quantum thermoelectric junctions, Phys. Rev. E **99**, 062141 (2019).
[116] O. Entin-Wohlman, Y. Imry, and A. Aharony, Three-terminal thermoelectric transport through a molecular junction, Phys. Rev. B **82**, 115314 (2010).
[117] R. Härtle and M. Thoss, Resonant electron transport in single-molecule junctions: Vibrational excitation rectification, negative differential resistance, and local cooling, Phys. Rev. B **83**, 115414 (2011).
[118] G. Schaller, T. Krause, T. Brandes, and M. Esposito, Single-electron transistor strongly coupled to vibrations: Counting statistics and fluctuation theorem, New J. Phys. **15**, 033032 (2013).
[119] L. Simine and D. Segal, Vibrational cooling heating, and instability in molecular conducting junctions: Full counting statistics analysis, Phys. Chem. Chem. Phys. **14**, 13820 (2012).
[120] B. K. Agarwalla, J.-H. Jiang, and D. Segal, Full counting statistics of vibrationally assisted electronic conduction: Transport and fluctuations of thermoelectric efficiency, Phys. Rev. B **92**, 245418 (2015).
[121] B. K. Agarwalla, J.-H. Jiang, and D. Segal, Thermoelectricity in molecular junctions with harmonic and anharmonic modes, Beilstein J. Nanotechnol. **6**, 2129 (2015).
[122] G. T. Landi, D. Poletti, and G. Schaller, Nonequilibrium boundary driven quantum systems: Models, methods, and properties, Rev. Mod. Phys. **94**, 045006 (2022).
[123] H. Schwager, J. I. Cirac, and G. Giedke, Dissipative spin chains: Implementation with cold atoms and steady-state properties, Phys. Rev. A **87**, 022110 (2013).
[124] M. Žnidarič, Relaxation times of dissipative many-body quantum systems, Phys. Rev. E **92**, 042143 (2015).
[125] A. Bose, Effect of phonons and impurities on the quantum transport in *XXZ* spin-chains, ArXiv:2206.11156.

[126] T. Prosen, Exact Nonequilibrium Steady State of a Strongly Driven Open *XXZ* Chain, Phys. Rev. Lett. **107**, 137201 (2011).

[127] G. T. Landi, E. Novais, M. J. de Oliveira, and D. Karevski, Flux rectification in the quantum *XXZ* chain, Phys. Rev. E **90**, 042142 (2014).

[128] E. Pereira, Heat work, and energy currents in the boundary-driven *XXZ* spin chain, Phys. Rev. E **97**, 022115 (2018).

[129] C. Gross and I. Bloch, Quantum simulations with ultracold atoms in optical lattices, Science **357**, 995 (2017).

[130] J. B. Brask, G. Haack, N. Brunner, and M. Huber, Autonomous quantum thermal machine for generating steady-state entanglement, New J. Phys. **17**, 113029 (2015).

[131] S. Khandelwal, M. Perarnau-Llobet, S. Seah, N. Brunner, and G. Haack, Characterizing the performance of heat rectifiers, ArXiv:2208.10809.